Several Novel Nuclear Envelope Transmembrane Proteins Identified in Skeletal Muscle Have Cytoskeletal Associations*[S]

Gavin S. Wilkie‡§, Nadia Korfali‡§, Selene K. Swanson¶, Poonam Malik‡‖, Vlastimil Srsen‡, Dzmitry G. Batrakou‡, Jose de las Heras‡, Nikolaj Zuleger‡, Alastair R. W. Kerr‡, Laurence Florens¶, and Eric C. Schirmer‡ ‡‡**

Nuclear envelopes from liver and a neuroblastoma cell line have previously been analyzed by proteomics; however, most diseases associated with the nuclear envelope affect muscle. To determine whether muscle has unique nuclear envelope proteins, rat skeletal muscle nuclear envelopes were prepared and analyzed by multidimensional protein identification technology. Many novel muscle-specific proteins were identified that did not appear in previous nuclear envelope data sets. Nuclear envelope residence was confirmed for 11 of these by expression of fusion proteins and by antibody staining of muscle tissue cryosections. Moreover, transcript levels for several of the newly identified nuclear envelope transmembrane proteins increased during muscle differentiation using mouse and human *in vitro* model systems. Some of these proteins tracked with microtubules at the nuclear surface in interphase cells and accumulated at the base of the microtubule spindle in mitotic cells, suggesting they may associate with complexes that connect the nucleus to the cytoskeleton. The finding of tissue-specific proteins in the skeletal muscle nuclear envelope proteome argues the importance of analyzing nuclear envelopes from all tissues linked to disease and suggests that general investigation of tissue differences in organellar proteomes might yield critical insights. ***Molecular & Cellular Proteomics 10: 10.1074/mcp.M110.003129, 1–16, 2011.***

The nuclear envelope (NE)[1] is an impenetrable membrane barrier between the nucleus and the cytoplasm perforated by nuclear pore complexes (NPCs) that regulate transport of soluble macromolecules in and out of the nucleus (1, 2). Structurally, the NE consists of the outer nuclear membrane (ONM) that is continuous with the endoplasmic reticulum (ER) (3), a lumen, the inner nuclear membrane (INM), and associated proteins including the NPCs and the intermediate filament nuclear Lamin polymer (4). Both the ONM and the INM have unique sets of transmembrane proteins, sometimes called NETs for nuclear envelope transmembrane proteins. Lamins and several NETs have been linked to an increasing number of relatively rare diseases that range from forms of muscular dystrophy to neuropathy, dermopathy, lipodystrophy, bone disorders, and accelerated aging syndromes (5, 6).

The three favored molecular mechanisms to explain NE disease pathology are mechanical instability from disruption of Lamin-cytoskeleton interactions, altered expression of genes regulated from the nuclear periphery, and disabling of the cell cycle/stem cell maintenance (6, 7). All of these may involve additional associated proteins to produce pathology. Indeed, it would seem that some proteins must be missing from the system as those so far mutated in disease are widely expressed, yet each disease exhibits pathology in a particular subset of the tissues in which the protein is expressed. Because both gene regulation and cytoskeletal connections have been implicated, NE proteins involved could reside in either the INM or the ONM.

The mechanical stability of the NE is derived largely from the nuclear Lamin polymer. Loss of Lamins (8–10) or their mutation (11) greatly disturbs nuclear morphology and stability. This stability itself varies among different cell types as, for example, neutrophils have highly lobulated nuclei and have higher relative concentrations of the Lamin B2 subtype (12), which is the least stable of the different Lamin subtypes (13, 14). In contrast, muscle cells must withstand high shear forces and have high concentrations of Lamin A, the most stable subtype. Many NETs bind Lamins, some of which also make connections across the lumen of the NE to

From the ‡Wellcome Trust Centre for Cell Biology, University of Edinburgh, Edinburgh EH9 3JR, United Kingdom and ¶Stowers Institute for Medical Research, Kansas City, Missouri 64110

Received, July 13, 2010, and in revised form, September 14, 2010
⌘ *Author's Choice*—Final version full access.
Published, MCP Papers in Press, September 27, 2010, DOI 10.1074/mcp.M110.003129

[1] The abbreviations used are: NE, nuclear envelope; NET, nuclear envelope transmembrane protein; INM, inner nuclear membrane; SR, sarcoplasmic reticulum; ONM, outer nuclear membrane; MudPIT, multidimensional protein identification technology; NPC, nuclear pore complex; ER, endoplasmic reticulum; EDMD, Emery-Dreifuss muscular dystrophy; qRT-PCR, quantitative RT-PCR; FDR, false discovery rate; NSAF, normalized spectral abundance factor; dNSAF, distributed normalized spectral abundance factor; CKM, creatine muscle kinase; MYOG, myogenin; MYH1, myosin heavy chain 1; Hs, homo sapiens; Mm, mus musculus.

ONM proteins (15), which in turn connect the NE to the cytoskeleton (16, 17).

Mutations in the *LMNA* gene encoding Lamins A and C cause forms of Emery-Dreifuss muscular dystrophy (EDMD) (18, 19), limb-girdle muscular dystrophy (LGMD-1B) (20), and dilated cardiomyopathy with conduction defect (CMD1A) (21), which each affect different muscle groups, although all are often also associated with cardiac conduction defects. Mutations in the transmembrane proteins Emerin and Nesprin 1 cause other forms of EDMD (22, 23). Nesprins have been shown to connect to cytoskeletal proteins (16, 17, 24, 25). Thus, both Lamins and NETs involved in connecting Lamins to the cytoskeleton can cause muscle disease in humans.

Postulating that other, more muscle-specific proteins might also contribute to NE-cytoskeleton interactions, we sought to determine whether additional NETs could be found in the NE proteome of skeletal muscle. The previously validated subtractive approach was applied (26) using microsomes/sarcoplasmic reticulum (SR) and mitochondria, the principal membrane contaminants expected, as subtractive fractions. Many new NE proteins were identified that had not been identified in previous NE proteomics investigations using liver, blood, and neuroblastoma cells (26–28). NE residence was confirmed for 11 novel NETs by expression of epitope-tagged versions and using antibodies on tissue cryosections.

Muscle-specific expression was determined for several NETs both according to transcriptome databases (29) and by direct testing with qRT-PCR. Moreover, some of the novel skeletal muscle NETs were up-regulated in myogenesis. Expression of NETs as tagged fusions revealed that NETs TMEM214 and KLHL31 concentrate at the nuclear surface with partial overlap with microtubules, suggesting some connectivity with the cytoskeleton. Moreover, TMEM214 and the NET WFS1 have a unique distribution at the base of the spindle poles in mitosis similar to that recently reported for NET5/TMEM201/Samp1 (30). Thus, some of these newly identified muscle NETs could potentially contribute to cytoskeletal defects in NE muscle diseases.

EXPERIMENTAL PROCEDURES

Preparation of Skeletal Muscle NEs and Microsomes/SR—Six to 10 week-old Sprague-Dawley rats were obtained from the University of Edinburgh animal facility according to university ethics procedures. For time and gradient size constraints, each individual preparation was limited to six rats. The procedure is given with full details in Ref. 31, but briefly, hind leg muscle between the femur and hip was isolated after discarding the sciatic nerve, and the muscle was crudely chopped into roughly 0.5-cm pieces, rinsed, and weighed. This was minced three times at 4 °C in 50 ml of ice-cold homogenization buffer (10 mM HEPES, pH 7.4, 60 mM KCl, 0.5 mM spermidine, 0.15 mM spermine, 2 mM EDTA, 0.5 mM EGTA, and 300 mM sucrose with freshly added protease inhibitors and 2 mM DTT) and then brought to a volume of 5 ml/g of starting muscle mass with homogenization buffer. A Potter-Elvehjem motorized Dounce homogenizer with a 0.1–0.15-mm-clearance Teflon pestle was used at 900–1000 rpm to produce a crude homogenate that was then poured through four layers of sterile cheesecloth on ice in a 4 °C room. Crude nuclei were pelleted from the filtrate at 1000 × *g* in a swinging bucket rotor for 10 min at 4 °C. The supernatant was carefully removed and processed for mitochondria and microsome/SR membranes (see below). The crude nuclear pellet was washed with Percoll gradient buffer (10 mM HEPES, pH 7.4, 60 mM KCl, 0.1 mM EDTA, 0.1 mM EGTA, and 300 mM sucrose), repelleted, and resuspended in 26.7 ml of ice-cold Percoll gradient buffer. Percoll (Sigma 77237) was added to a final concentration of 27% (v/v), and nuclei were pelleted at 27,000 × *g* for 30 min at 4 °C in a swinging bucket rotor. Some fragmented myofibrils have a mass similar to that of nuclei but a different density, so the isopycnic gradient accumulates them at the top (32). Nuclei were collected from where they banded near the bottom of the tube. Fractions were checked for nuclear enrichment by microscopy. The nuclear fraction was diluted 10-fold with ice-cold SHKM buffer (50 mM HEPES, pH 7.4, 25 mM KCl, 5 mM $MgCl_2$, 1 mM DTT, and 0.25 M sucrose) and pelleted by centrifugation at 4000 × *g* for 20 min at 4 °C in a swinging bucket rotor. This pellet still contains other membrane and cytoplasmic contaminants, so the pellets were resuspended in 11 ml of ice-cold SHKM buffer using a hand-held Dounce homogenizer. 39 ml of SHKM buffer with 2.3 M sucrose was added to bring the sucrose concentration to 1.85 M. 25 ml was removed to each SW28 ultracentrifuge tube and underlaid with 5 ml of ice-cold SHKM buffer with 2.15 M sucrose and then a further 5 ml of SHKM buffer with 2.8 M sucrose using a 14-gauge needle. After centrifugation in an SW28 swinging bucket rotor for 60 min at 82,000 × *g* at 4 °C, the nuclei occur at the interface of the 2.8 and 2.15 M sucrose layers. Nuclei were collected, diluted 10-fold in SHKM buffer, centrifuged at 4000 × *g* for 20 min at 4 °C, and then resuspended in SHKM buffer, and nuclei were counted using a hemocytometer. At this stage, no contaminants could be observed under the microscope.

NEs were then prepared from isolated nuclei by two rounds of digestion with DNase I (Sigma D4527) and RNase A (Sigma R4875) in 0.3 M sucrose, 10 mM HEPES, pH 7.4, 2 mM $MgCl_2$, 0.5 mM $CaCl_2$, and 2 mM DTT (using a Dounce homogenizer to resuspend nuclei) for 20 min followed by layering onto the same buffer with 0.9 M sucrose and centrifugation at 4000 × *g* for 10 min at 4 °C to wash out and float digested chromatin. The first round used nuclei at 1–2 million/ml with 10 units/ml DNase and 1.4 mg/ml RNase, and the second round used nuclei at 2–4 million/ml with 50 units/ml DNase and 5 mg/ml RNase. Digestions were followed by rapid staining of nuclei with 4,6-diamidino-2-phenylindole dihydrochloride (DAPI) using a fluorescence microscope and extended if most of the DAPI signal had not been washed out. NEs were snap frozen in liquid nitrogen and maintained at −80 °C.

To prepare mitochondria and microsomes enriched in SR membranes, 0.5 mM EDTA was added to the postnuclear supernatant to inhibit metalloproteases. This homogenate was first centrifuged at 10,000 × *g* at 4 °C for 20 min to pellet mitochondria. The postmitochondrial supernatant was then subjected to centrifugation at 100,000 × *g* for 45 min at 4 °C to generate a crude microsomal/SR pellet. This was resuspended in 5 ml of ice-cold SHKM buffer, and the sucrose concentration was increased to 2 M by adding 2.7 volumes of ice-cold 2.8 M SHKM buffer. 28 ml of these membranes was added to SW28 ultracentrifuge tubes and overlaid with 7 ml of ice-cold SHKM buffer with 1.85 M sucrose and again with 3 ml of regular SHKM buffer. Microsomes were floated at 57,000 × *g* for 4 h at 4 °C in an SW28 swinging bucket rotor. Microsomes were recovered by aspiration of material at the interphase between the 1.85 M sucrose layer and the uppermost 0.25 M sucrose layer, diluted with 4 volumes of SHKM buffer, and pelleted at 152,000 × *g* in a 45 Ti rotor for 75 min.

NE preparations were accumulated and divided into aliquots. One aliquot was extracted on ice with 400 mM NaCl, 25 mM HEPES, pH 8.0, 5 mM $MgCl_2$, 10 mM DTT, and 1% β-D-octyl glucoside. A separate NE aliquot and a microsomal membrane aliquot were extracted with

0.1 N NaOH and 10 mM DTT. The material used for mass spectrometry was pelleted from the extracted material by centrifugation at 150,000 × *g* for 30 min and washed three times in filtered H_2O prior to digestion.

MudPIT—Two biological replicate preparations of NaOH-extracted NEs and SR were analyzed in duplicate, whereas two technical replicates were obtained for one preparation of salt- and detergent-extracted NEs (Table I and supplemental Table S1). Pellets were solubilized in 0.1 M Tris-HCl, pH 8.5, 8 M urea, and 5 mM tris(2-carboxylethyl)phosphine hydrochloride. Next, free cysteines were alkylated with 10 mM iodoacetamide for 30 min, and Endoproteinase Lys-C (Roche Applied Science) was added at a 1:100 (w/w) enzyme to protein ratio for 6 h at 37 °C. Urea was diluted to 2 M with 0.1 M Tris-HCl, pH 8.5, and $CaCl_2$ (0.5 mM) and modified Trypsin (1:100, w/w) were added for 12 h at 37 °C. Digestions were quenched with 5% formic acid (33). Samples were centrifuged for 30 min at 17,500 × *g*. Supernatants (Ti Table 1) were directly analyzed by MudPIT, whereas pellets were further resuspended in 0.1 M sodium carbonate (Na_2CO_3), pH 11.5, 8 M urea, and 5 mM tris(2-carboxylethyl)phosphine hydrochloride for 30 min; incubated with 10 mM iodoacetamide for 30 min; and then further digested with Proteinase K for 4 h at 37 °C and separately analyzed by MudPIT (34).

MudPIT was performed as described previously (35) using a 200–300 nl/min flow rate over 12–15 cycles (Table I and supplemental Table S1) of 120 min each of increasing salt concentrations followed by organic gradients (5–80% acetonitrile with 0.1% formic acid) (35). The last two to five chromatography steps consisted of a high salt wash with 5% acetonitrile, 0.1% formic acid, and 500 mM ammonium acetate followed by the acetonitrile gradient. Distal application of a 2.5-kV voltage electrosprayed eluting peptides directly into a linear ion trap mass spectrometer (ThermoFinnigan). Each full MS scan (from 400 to 1600 *m/z*) was followed by five MS/MS events using data-dependent acquisition (at 35% collision energy). The raw mass spectrometric data may be downloaded from proteomecommons.org Tranche using the hash identifiers provided in Table I and supplemental Table S1.

RAW files extracted into ms2 file format (36) using RAW_Xtract v.1.0 (37) were queried for peptide sequence information using SEQUEST v.27 (revision 9) (38) against 28,400 rat proteins (non-redundant NCBI sequences on July 10, 2006) plus 197 human and mouse homologs of previously identified NETs (26) and 172 sequences from usual contaminants (*e.g.* human keratins). To estimate false discovery rates, each non-redundant protein entry was randomized and added to the database, bringing the total search space to 57,538 sequences (supplemental Table S1). MS/MS spectra were searched without specifying differential modifications, but +57 Da were added statically to cysteine residues to account for carboxamidomethylation. No enzyme specificity was imposed during searches, setting a mass tolerance of 3 amu for precursor ions and of ±0.5 amu for fragment ions.

Different runs were compared using DTASelect and Contrast (39). Spectrum/peptide matches were retained if at least 7 amino acids long with ends complying with proteolytic specificity. Other criterion were ΔCn ≥ 0.08; XCorr ≥ 1.8 for singly, 2.0 for doubly, and 3.0 for triply charged spectra; and a maximum Sp rank of 10. For Proteinase K-digested samples, no specific peptide ends were imposed, but the ΔCn cutoff was increased to 0.15 (40), whereas XCorr minima were increased to 2.5 for doubly and 3.5 for triply charged spectra (SEQUEST parameters for the spectrum to peptide matches for all detected proteins are provided in supplemental Table S2). Peptide hits were merged from all analyses to establish a master list of proteins identified by at least two peptides or one peptide with two independent spectra. In addition, six previously described liver and blood NETs as well as three newly characterized skeletal

TABLE I

Hash identifiers to access raw mass spectrometry files for each MudPIT run

Individual runs are organized by cell fraction (NE or SR), extraction (NaOH or salt/detergent (SD)), and protease (Trypsin (Ti) or Proteinase K (PK)) to generate peptides for analysis.

At https://www.proteomecommons.org/tranche/downloads.jsp the raw mass spectrometry files can be downloaded using the following hash identifiers. In all cases, there are two files ranging from 100 MB to 1.5 GB that are archived and compressed tar.gz files: use tar —xzf linux command to uncompress to *.RAW files (1 per MudPIT step)	Description of Tranche (run name used in supplemental tables)
U4oMnK/mHWCdGJ8KpNw5iv2ZPYyxYeVOvNzuYOQ9A7qrBmtMNy1dCO7Kbpmjj0WN0fvJSyhOBK0rbDCYIPvyq33KHbYAAAAAAAAFkg==	RnNaOH-NE_muscles_Ti_1
eHaU1zhkwqfSFMUO4UEkzUFbJPw6vyS45tO318icJJGuYWHjUMK/11UF8+COjwqVrdOf9JrS6ma3WSBSgTBJQAqykMMAAAAAAAAFIA==	RnNaOH-NE_muscles_Ti_2
QVcyypxCuUz96X63QHoyirM3VMeo7Z7CmAUOCxR+kt1Rk/N0HF95t9n1Ik/nlla4pFMAawYyaKRQYxYCHEwqLFyVcWoAAAAAAAAGZQ==	RnNaOH-NE_muscles_PK_1
JFoLKqlkxRP2oX97exWAW80opnPuqRPvaDv72NMWJ8hSeMs8bIERnXOFC/nKhbB8INlKMcXlo09rESd1 × 5bskRSVepAAAAAAAAAFlQ==	RnNaOH-NE_muscles_Ti_3
LxSuw9vAbjDC/bWD2ZO3wf+Ypt5gp+SKVJMncZZxpCvFgbLSRGlzbL0vovsfmWLUo2DuLKyCudi4v9anLRg0k6JoqBUAAAAAAAAAFjQ==	RnNaOH-NE_muscles_Ti_4
39VSpfd6gB1OtpV5LTY6Wu7MxEBUwvjGF8ixiUE0nZR2l8QCbl21e0PZpOwnhKH3HwNv+ToF8AaWm18iUVegCFPrVKQAAAAAAAAAFeg==	RnSD-NE_muscles_Ti_1
4p8SXlJPyzBw5yVMEQVPAHONj7H8neFm4BD9bC+dL5XNsYTo4sllmyBpwpPMrlHy++HM6So6odAATGlzmP5G3TDqgwwAAAAAAAAAFeg==	RnSD-NE_muscles_Ti_2
anQNY4xCeTOsKvMrdqopEgAh9rja7xmYNC/mGwN6wumhDqUMCf5AbFGgDY4I6AGPpQziUJE9NiG5Kpmj3TkpzQUhlWgAAAAAAAAFkA==	RnNaOH-SR_muscles_Ti_1
aDpnQPjyNEgCqiN6Onra9dqzBDKWkQD9btbY8ye3gZAxVdFSGM9ddqr+Od7/a+Gx8/qdENJij2OlPbtsUfD2lBjTTS0AAAAAAAAAFkA==	RnNaOH-SR_muscles_Ti_2
nOl0FKF+b+56faEzU+sMQwEd46id4tTQlk1N/hhl1kWOezoF9HtAyXiQGcbY5bQgxZhrv/xGGslPQTga7G2gJYPlczcAAAAAAAAGZA==	RnNaOH-SR_muscles_PK_1
JZMpidblCAlMpTaUDeiiZdSpbAmm4L8SH7w2xB83m2LtAjPtz0cTrbe1XcCBm1smSjUH5T6PWj4fZZFV5kGcyC3ZELoAAAAAAAAAFkQ==	RnNaOH-SR_muscles_Ti_3
xTESWmC9cv1UKXyctOVK35MKMTH7Iw5XZ0rv9n5BefVgOM32ubzLabhUHDQC1TBhxtlCZsSyqw9N7IWXR3/UqmHXq0MAAAAAAAAAFkQ==	RnNaOH-SR_muscles_Ti_4
CT5hCf/Y3/wzsYaPfsoNZ75InelvcN+arCYacOxlOb0+OgLXno5a3nRhlGbzK/ckuCtAwQwXpOk6lcPZFk5WMAJRf4UAAAAAAAAGYQ==	RnNaOH-SR_muscles_PK_2

muscle NETs were manually selected although detected by single peptides (annotated spectra for these proteins are provided in supplemental Fig. S1). Based on the merged detected peptides, proteins could fall into three categories following the parsimony principle. (i) Proteins detected by the exact same set of peptides were grouped together because they could not be distinguished based on the available peptide data (see column named "Proteins in Group" in supplemental Table S3), and only one arbitrarily selected representative protein entry is reported for such groups of proteins (see column labeled "Locus" in supplemental Table S3). (ii) Proteins with at least one peptide uniquely mapping to them were considered unique entries. (iii) Subset proteins for which no unique peptides were detected were removed from the final list of identified proteins.

Identifications mapping to shuffled peptides were used to estimate false discovery rates. Spectral FDR was calculated as shown in Equation 1.

$$\text{Spectral FDR} = \frac{2 \times \text{SHUFFLED\_SpectralCounts}}{\text{Total\_SpectralCounts}} \times 100 \quad \text{(Eq. 1)}$$

Protein level FDR was calculated as shown in Equation 2.

$$\text{Protein FDR} = \frac{\text{SHUFFLED\_Proteins}}{\text{Total\_Proteins}} \times 100 \quad \text{(Eq. 2)}$$

Under these criteria, the final FDRs at the protein and peptide levels were on average 2.2 ± 0.9 and 0.3 ± 0.09%, respectively (supplemental Table S3).

Normalized spectral counts (NSAF) were calculated for each nonredundant protein to estimate relative protein levels as described (41–43).

$$(\text{NSAF})_i = \frac{(\text{SpectralCount/Length})_i}{\sum_{k=1}^{N} (\text{SpectralCount/Length})_k} \quad \text{(Eq. 3)}$$

To refine spectral counts to deal with peptides shared between multiple proteins (44), dNSAFs were calculated based on distributed spectral counts for each run in which shared spectral counts were distributed based on spectral counts unique to each isoform (supplemental Table S3). For each protein, averaged dNSAF and standard deviations (supplemental Table S3) were calculated across several replicate analyses of NE and SR samples (supplemental Table S1).

Bioinformatics Analysis—Proteins were mapped to an Ensembl gene to remove redundancy from differences in protein annotations and cross-referenced to the human genes with Ensembl release 48 (45). Orthologous group identities were sorted according to frequency of detection in the NE and microsome runs, relative levels (determined by averaged dNSAF values), membrane helix prediction (determined using TMHMM 2.0; http://www.cbs.dtu.dk/services/TMHMM-2.0/; Ref. 46), and dNSAF ratios between values measured in NEs *versus* microsomes/SR (supplemental Table S3). Biologically interesting gene ontology terms were retrieved from the mySQL database (http://amigo.geneontology.org; Ref. 47) and added to tables. Comparison of expression levels in different tissues was done by downloading relative values from BioGPS (http://biogps.gnf.org/#goto=welcome; Refs. 29 and 48) and calculating the -fold expression over the median value from a wide variety of mouse tissues tested in this transcriptome database.

Plasmid Construction—IMAGE clones for human NETs *TMEM38A*, *TMEM194*, *POPDC2*, *KLHL31*, *WFS1*, *TMEM70*, *MBOAT5*, *CKAP4*, *TMEM214*, *RHBDD1*, and *TMEM201* were obtained from RZPD and Geneservice. Coding sequences were amplified by PCR with added 5′ and 3′ restriction sites, sequenced from both ends in intermediate cloning vectors, and then inserted into mammalian expression vector pEGFP-N2 (Clontech) or pmRFP-N2 (derived from pEGFP-N2 by replacing the GFP coding sequence with that of monomeric red fluorescent protein). *Sec61β-GFP* was obtained from Tom Rapoport (Harvard, Boston, MA).

Antibodies and Western Blotting—Antibodies used were glyceraldehyde-3-phosphate dehydrogenase (GAPDH) (Enogene E1C604), Calreticulin (Cell Signaling Technology 2891S), Calnexin (Stressgen SPA-860), Lamin A (3262; Ref. 11), Nup153 (Covance MMS-102P), Nup358 (raised against recombinant human protein amino acids 2595–2881; a kind gift from F. Melchior), SUN2 (Millipore 06-1038), Tubulin (Sigma T6074), TMEM38A (Millipore 06-1005), POPDC2 (Millipore 06-1007), TMEM201 (Millipore 06-1013), and LOC203547 (Millipore 06-1008). All fluorophore-conjugated secondary antibodies were minimally cross reactive from donkey (Jackson ImmunoResearch Laboratories) or goat (Molecular Probes).

Mitochondria prepared as described above were directly lysed in sample buffer. Muscle NE and microsomes/SR were incubated on ice in 50 mM Tris-HCl, pH 7.4, 150 mM NaCl, 2 mM MgCl2, and 0.2% Nonidet P-40 with protease inhibitors; then heated at 65 °C for 2 min; and sonicated in a 4 °C sonic bath. Protein concentrations were determined by Bradford assay before adding sample buffer. Mitochondrial loading was based on Coomassie staining compared with NE and SR lanes.

All blots shown were run according to standard procedures, and protein bands were visualized and quantified with IR800-conjugated secondary antibodies using a LI-COR Odyssey imaging system and software (Odyssey 3.0.16) using median background subtraction. For Fig. 2, example blots are shown, whereas for Fig. 5, a graph from averages of three independent blots for each NET and controls is presented.

Cell Culture, Differentiation, and Transient Transfection—HT1080, HeLa, U2OS, RD, and C2C12 cells were maintained in high glucose DMEM (4.5 g/liter glucose; Invitrogen) supplemented with 10% fetal bovine serum (FBS), 100 μg/μl penicillin, and 100 μg/μl streptomycin sulfate (Invitrogen). RD and C2C12 cells were differentiated after 2 days of confluence by replacing the medium with 0.2% FBS medium containing 10 μg/ml 12-*O*-tetradecanoylphorbol-13-acetate and 0.1% FBS medium containing 5 μg/ml insulin and 5 μg/ml transferrin, respectively. Successful differentiation into myotubes was confirmed by light microscopy, counting that more than half of cell bodies exhibited the lengthening characteristic of myotubes and were multinucleate. Cells were extracted for RNA typically 2–3 days after myotubes became prevalent. Adherent cells destined for microscopy were plated on coverslips, and when indicated, DNA was transfected the next day using FuGENE 6 (Roche Applied Science) according to the manufacturer's instructions.

Immunofluorescence Microscopy—After 30 h post-transfection, cells were directly fixed for 7 min in 3.7% formaldehyde and processed for microscopy after permeabilization for 6 min in 0.2% Triton X-100. For the prefixation extractions in Fig. 5, cells were first washed with PBS; then extracted for 1 min with 1% Triton X-100, 25 mM Tris, pH 8.0, 150 mM KOAc, 15 mM NaCl, and 5 mM $MgCl_2$; washed again with PBS; and then fixed with formaldehyde. In both cases, cells were then blocked with 10% FBS and 200 mM glycine in PBS and incubated for 40 min at RT with relevant antibodies. DNA was visualized with Hoechst 33342 or DAPI, and coverslips were mounted in Fluoromount-G (EM Sciences). Most images were obtained using a Nikon TE-2000 microscope equipped with a 1.45 numerical aperture 100× objective, PIFOC Z-axis focus drive (Physik Instruments), Sedat quad filter set, and CoolSnapHQ High Speed Monochrome charge-

coupled device camera (Photometrics). Those in Fig. 4*A* were deconvolved from 0.2-μm sections using AutoquantX. Structured illumination images in Fig. 4*B* were taken on the OMX system at the University of Dundee microscopy facility, and Alexa Fluor secondary antibodies (Molecular Probes) were used (other details are available upon request).

For cryosections, fresh rat heart or leg muscle was cut into 2–3-mm cubes, embedded in optimal cutting temperature compound (Tissue-Tek), snap frozen in liquid nitrogen, and maintained at −80 °C. Sections were cut on a Leica CM 1900 cryostat at 6–8-μm thickness and fixed in −20 °C methanol. After rehydration, sections were incubated with NET antibodies overnight at 4 °C followed by secondary antibodies as above. Cryosection images were recorded using an SP5 confocal system (Leica) with 63× oil 1.4 numerical aperture objective using argon and UV lasers. Micrographs were saved from source programs as .tif files and prepared for figures using Photoshop 8.0.

Electron Microscopy—Isolated skeletal muscle NEs were fixed in 3% glutaraldehyde in 0.1 M sodium cacodylate, pH 7.3, for 2 h; washed in 0.1 M sodium cacodylate; postfixed in 1% osmium tetroxide for 45 min; washed again; and dehydrated in 50, 70, 90, and 100% normal grade acetones for 10 min each and then for a further two 10-min changes in analar acetone. Samples were then embedded in Araldite resin. 60-nm-thick sections were cut on a Reichert OMU4 ultramicrotome (Leica), stained in uranyl acetate and lead citrate, and then viewed in a Phillips CM120 transmission electron microscope. Images were taken at 100 kV at 11,000× magnification using a Gatan Orius charge-coupled device camera.

Semiquantitative and Quantitative RT-PCR—For differentiation experiments, cells were lysed with TRI Reagent (Sigma), and total RNA was extracted according to the manufacturer's instructions from C2C12 or RD myoblasts or 4-day differentiated myotubes. RT-PCRs were carried out with 100 ng of total RNA using the Titan one-tube RT-PCR system (Roche Applied Science) in accordance with the manufacturer's instructions except that the dNTP concentration was increased to 500 μM and $MgCl_2$ was increased to 3 mM. Typical reaction conditions were 30 min of reverse transcription at 50 °C; 2 min of denaturation at 94 °C; and then 24 cycles of 94 °C for 30 s, 60 °C for 30 s, and 68 °C for 45 s. Peptidylprolyl isomerase A (*PPIA*) was used as a loading control, and creatine muscle kinase (*CKM*), myogenin (*MYOG*), and myosin heavy chain 1 (*MYH1*) were used as positive controls. Human (Hs) and mouse (Mm) primer sets used are given in supplemental Table S4.

For tissue expression experiments, human tissue RNAs were purchased from Stratagene except for blood RNA that was prepared from peripheral blood mononuclear cells isolated from buffy coats obtained from the Scottish National Blood Transfusion Service. 8 μg of RNA from each tissue was first converted into cDNA using a First Strand cDNA Synthesis kit (Thermoscript, Invitrogen) using a mixture of reverse primers for the cDNA to be amplified at a final concentration of 3 μM. The quantitative real time RT-PCR control was *CKM* in heart muscle. Standard curves were performed using a Roche Lightcycler for each primer pair by serial dilutions of cDNA products of heart muscle (1:5, 1:25, 1:125, and 1:625) to estimate PCR efficiency. *GAPDH* was used as the internal control to normalize the cDNA samples across the different tissues, and the relative abundance of each mRNA within the tissues was calculated using heart as the standard reference dilution. To avoid amplification of contaminating genomic DNA, primers from each set were specific to different exons. Primers used are given in supplemental Table S4.

RESULTS

Generation of Muscle NE Fractions—Rat leg muscle nuclei were prepared using a method that first depleted collagen from crude lysates (confirmed by Western blot; data not shown), thus presumably removing most connective tissue and enriching for myofiber nuclei. Myofibrillar material and contaminating membranes were then removed on Percoll and sucrose gradients (31) (Fig. 1, *A* and *B*). Isolated nuclei were subsequently digested with DNase and RNase and salt-washed to remove most of the nuclear contents (Fig. 1*C*). Even after such isolation, NEs maintain strong connections to various protein partners including a fraction of peripheral chromatin as shown by electron microscopy (Fig. 1*D*). Therefore, to further purify NEs prior to mass spectrometry analysis, NE fractions were extracted with 1% β-octyl glucoside and 400 mM NaCl or with 0.1 N NaOH (Fig. 1*A*), which enrich for proteins associated with the insoluble intermediate filament Lamin polymer and integral membrane proteins, respectively. Both extracted fractions were separately analyzed (supplemental Table S1) because previous NE proteome analyses demonstrated that some well characterized NETs are distributed to one or the other fraction (26, 27).

Microsomes enriched in SR were separately prepared as a comparative/subtractive fraction. Some SR would be expected to contaminate NEs because the ONM is continuous with the SR, and also during nuclear isolation, some SR vesicles may stick to the surface of nuclei. In contrast, as nuclei are stable and pellet fully at low speeds, there should be no NE contamination in the microsome/SR fraction. Indeed, neither Lamins A/C nor the NET LAP2β, used as NE markers, were observed in the SR fraction by Western blot analysis (Fig. 2, *A* and *B*). Therefore, as the only membrane in the nucleus is the NE, all membrane proteins enriched in the NE fractions compared with the SR fractions should be true NETs. As expected, there were similar levels of the SR protein Calnexin in NE fractions because half of the NE, the ONM, is continuous with the SR (Fig. 2*B*). Mitochondria are also expected to stick to NEs during isolation, although most should in theory be removed by Dounce homogenization and sucrose gradients that float many contaminating membranes (Fig. 1*A*). Indeed, just as the NE Lamin A/C proteins were undetectable in a separately prepared mitochondrial fraction, the mitochondrial protein Porin was not detectable in the crude NE fraction (Fig. 2*C*).

As the vast majority of material was lost in isolating clean NEs from the skeletal muscle, NEs isolated from at least 15 separate preparations were combined prior to alkali or salt/detergent extraction. Thus, variation between preparations should have been averaged out.

MudPIT Analysis—After extraction, pellets of isolated NE fractions were digested with Endoproteinase Lys-C and Trypsin. Because some membrane proteins that associate with the intermediate filament Lamin polymer resist extraction with 2% Triton X-100 and 2 M NaCl, and the polymer itself is not completely solubilized even in 8 M urea, a second digestion was performed on material that remained insoluble after the Endoproteinase Lys-C and Trypsin digestion. Thus, material that could be pelleted at 17,500 × *g* for 30 min was subse-

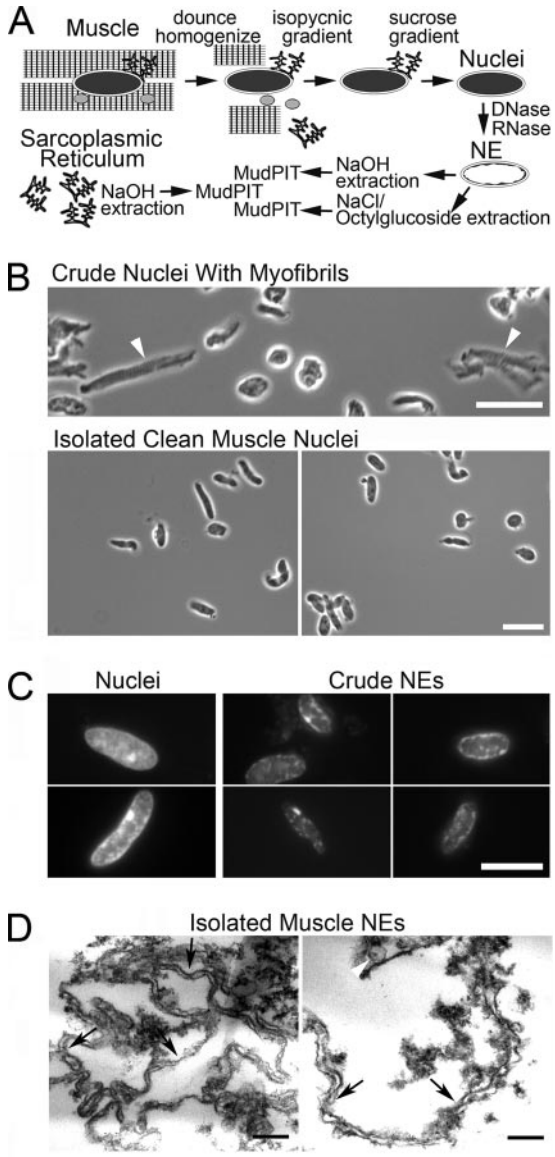

FIG. 1. **Cellular fractionation of rat muscle.** *A*, method schematic. Nuclei were first prepared from diced and homogenized rat leg muscle and cleaned of contaminating cellular structures by centrifugation first on isopycnic gradients and then on sucrose to float contaminating membranes while pelleting the denser nuclei. Crude NEs were prepared by digesting/extracting nuclear contents from isolated nuclei. Before MudPIT analysis, these were further extracted with 1% β-octyl glucoside and 400 mM NaCl or with 0.1 N NaOH to enrich for proteins associated with the insoluble Lamin polymer and integral membrane proteins, respectively. Microsomes/sarcoplasmic reticulum preparations were generated separately and analyzed for comparison/subtraction as they contain most expected membrane contaminants of the NE. *B*, *top panel*, before running both gradients, the crude nuclear fractions contained many chunks of myofibrillar material (*e.g.* Z-bands; highlighted with *white arrowheads*) released during homogenization. *Bottom panels*, after both gradients, isolated nuclei were clean of these contaminants. Phase-contrast light microscope images are shown. *Scale bar*, 10 μm. *C*, enrichment for NEs by chromatin digestion. DAPI staining for DNA visualizes significant nuclear chromatin content in an isolated muscle nucleus (*left panels*) and the loss of most of this material after two rounds of digestion with DNase and RNase each followed by salt washes (*two right panels*). Fluorescence microscope images are shown. *Scale bar*, 5 μm. *D*, ultrastructure of isolated NEs. Electron micrographs of crude muscle NEs show that most material in the population has the characteristic double membrane structure of the NE with little contamination from single membrane vesicles (a likely SR single membrane vesicle contaminant is highlighted by the *white arrowhead*). *Arrows* point to positions of NPCs. These NEs were further salt/detergent- or alkali-extracted prior to analysis by MudPIT. After such treatment, no structure remains that can be readily discerned by EM with the characteristics of NEs. *Scale bar*, 0.2 μm.

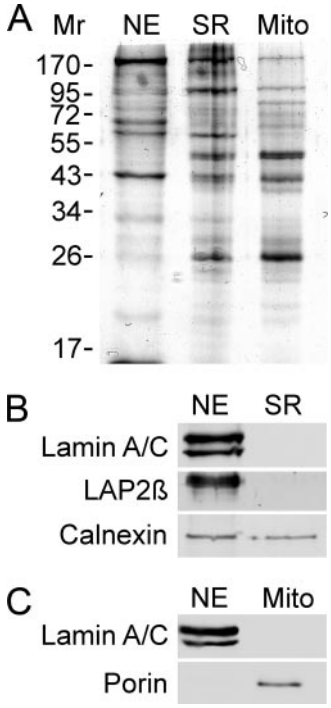

FIG. 2. **Fraction purity.** *A*, Coomassie-stained gel of NE and microsome/SR muscle fractions analyzed and also of a separately isolated muscle mitochondrial fraction (*Mito*). *B*, the SR marker Calnexin was present in both the SR and NE fractions because the ONM is continuous with the SR and shares many proteins. In contrast, the SR fraction was completely free of NE-specific markers, the NET LAP2β and Lamins A/C. Loading was the same as for *A* with similar amounts of total protein loaded. *C*, the mitochondrial marker Porin was absent from NEs, whereas Lamins A/C were absent from mitochondria. Loading was the same as in *A* and *B*.

quently digested with Proteinase K at high pH (34). The results of each digestion and replicates can be compared in supplemental Table S3. Five separate MudPIT runs were performed for NaOH-extracted NEs (one with Proteinase K digestion), and two were performed for the salt/detergent-extracted NEs. Six MudPIT runs were performed on the SR material extracted with NaOH (two with Proteinase K digestion). Thus, using different extraction conditions and different digestions and performing multiple runs were expected to provide comprehensive coverage to identify all proteins in the

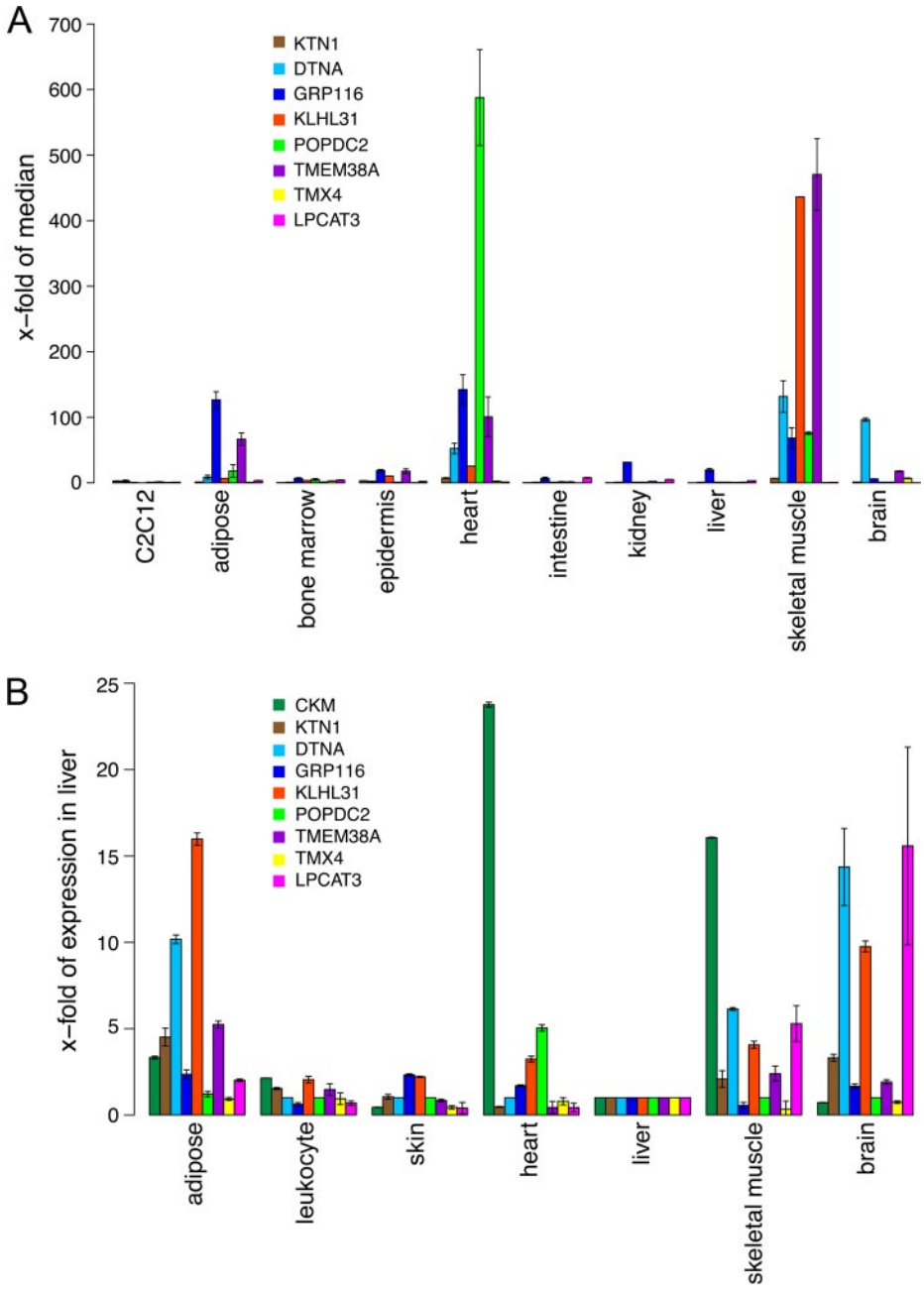

FIG. 3. **NET tissue specificity of expression.** *A*, expression data were downloaded from the BioGPS transcriptome database that compared over 60 mouse tissues on microarrays. The median expression value was obtained over the complete set of tissues, and data for a subset of tissues are graphed relative to this median value. Of the novel muscle putative NETs represented on the arrays, only one was not expressed notably above the median value in either heart or skeletal muscle (*LPCAT3*) with six expressed more than 100-fold over the median. In many cases, the median value occurred at background levels of expression (see Table II), so NETs that tended to be expressed around the median in most tissues besides muscle are more uniquely expressed in muscle. Error bars are standard deviations from fluorescence values from multiple microarrays. *B*, quantitative real time PCR of the same NETs and the control *CKM* over a smaller set of tissues. The values were generated in relation to *GAPDH* expression in the same reactions, and each NET is graphed as the -fold expression over its levels in liver. Tissue-preferential expression was also observed for several NETs directly tested by qRT-PCR; however, expression was sometimes observed in tissues that were at background levels according to the transcriptome data. Of particular note, *LPCAT3*, the only NET that was not up-regulated in skeletal muscle or heart according to transcriptome data, was up-regulated in skeletal muscle more than 5-fold by qRT-PCR. The expression of these new muscle NETs in blood and liver was at low/background levels by both methods, consistent with their having been uniquely identified in the skeletal muscle NE. Error bars are standard deviations from 3 Q-RT PCR replicates.

skeletal muscle NE. A total of seven MudPIT runs were acquired on the NE fractions because we postulated that some tissue-specific NETs might not be highly abundant. To test this, the frequency of NET detection of the seven NE runs was plotted against an estimate of abundance based on normalized spectral counts (dNSAF) (42, 44). A clear relationship was observed with the more abundant NETs tending to be detected not only in multiple analyses of the same tissue but also in independent analyses of different tissues (supplemental Fig. S2).

After removing redundancy by converting protein identities to orthologous gene groups, 1267 proteins were identified in total for the skeletal muscle NE data sets (supplemental Table S3). Separately, 1408 proteins were identified in the SR data sets (supplemental Table S3). Although fractions appeared to be clean of mitochondria by Western blot analysis, to more fully test mitochondrial contamination, data sets were compared with lists of mitochondrial proteins from a previous mass spectrometry study of that organelle (49) (supplemental Table S3). After subtracting 74 proteins that were previously identified in mitochondria, 1193 proteins remained in the skeletal muscle NE fraction. Using microsomes/SR strictly as an absolute subtractive fraction would have resulted in the loss of several well characterized

NETs including LBR, Emerin, SUN2, and Nesprin 1 (50–54). To some degree this is expected; for example, Emerin is not unique to the INM, and separate functions have been reported in the ONM, ER, and interstitial discs (55–57). Furthermore, a recent proteomics study suggests that at least a third of all proteins have multiple cellular localizations (58). Nonetheless, the number of spectra recovered from NEs was much greater than for ER for all the previously characterized NETs. Adding spectra from all runs, LBR had only two spectra recovered from the SR fraction compared with 94 from the NE fraction, Emerin had one in the SR compared with 33 in the NE fraction, SUN2 had 24 in the SR compared with 1490 in the NE, and Nesprin 1 had two in the SR compared with 281 in the NE (supplemental Table S3). Thus, instead of absolute subtraction, proteins were ordered according to their dNSAF estimate of abundance (42, 44), and NE data sets were restricted to those proteins either not detected in the microsomes or at least 5× more abundant than in the microsome fractions based on their NSAF values, which, again after subtracting all mitochondrial proteins, left 710 proteins in the skeletal muscle NE fraction (supplemental Table S3).

This protein set includes not only membrane proteins but also many soluble proteins. Some of these soluble proteins may have binding sites throughout the nucleus but nonetheless have relevant interactions at the NE. In contrast, the subset of proteins harboring transmembrane spans (NETs) is the most likely to be enriched at the NE and constitutes the surest core NE components. This set of proteins include all 13 of the original well characterized NETs, which were ubiquitously detected in our large scale analyses of nuclear envelopes isolated from liver (26), blood (28), and now muscle; these ubiquitous NETs were also recovered at high levels (dNSAF values) and reproducibly in multiple analyses of muscle NE (supplemental Fig. S2A and Table S5). An additional 28 liver NETs had been previously detected in liver NE data sets (26), 14 of which have confirmed NE residence (supplemental Fig. S2B and Table S5). Another 109 proteins were predicted to contain at least one transmembrane domain by TMHMM v2.0 or membrane anchor by SignalP. Some of the transmembrane proteins identified in the data sets were known proteins that had not been detected previously at the NE, many being ion transporters that likely function in muscle SR. Others had no annotations at the time of data set generation, and we selected 53 of these as putative novel NETs, 24 of which were also detected in a concurrent proteomics analysis of NEs from peripheral blood leukocytes (Ref. 28; supplemental Fig. S2C and Table S5). Within the "muscle-only" muscle NETs, one protein of high abundance was detected in six of seven runs (TMEM38A), another group of 11 proteins of lower abundance was detected in at least two runs, whereas 21 proteins were detected only once and at the lowest levels (supplemental Fig. S2D and Table S5). The nuclear envelope targeting of over half of the proteins (48 of 94) plotted in supplemental Fig. S2 has been confirmed. In

TABLE II

NETs with high expression levels in muscle tissues expressed as normalized microarray intensity units and relative to median (in parentheses) for all tissues sampled (see "Experimental Procedures")

Bold values, >10× median.

NET	Tissue of highest expression (Hs)	Hs heart	Hs skeletal muscle	Hs smooth muscle	Tissue of highest expression (Mm)	Mm heart	Mm skeletal muscle	Mm liver	C2C12
WFS1	Lung (8.0)	93.45 **(11.8)**	4.9 (0.6)	14.2 (1.8)	Nucleus accumbens (210.5)	1815.1 (8.6)	923.4 (4.4)	211.2 (1.0)	513.5 (2.4)
POPDC2	Heart (5.3)	194.6 **(36.7)**	16.3 (3.1)	5.85 (1.1)	Heart (4.6)	2703.8 **(583.2)**	350.3 **(75.6)**	4.6 (1.0)	4.6 (1.0)
KLHL31	Below threshold	—[a]	—	—	Skeletal muscle (70.4)	1792.4 **(25.5)**	30702.1 **(436.1)**	71.6 (1.0)	[b]
GPR116	Fetal lung (6.7)	8.7 (1.3)	9.6 (1.4)	6.8 (1.0)	Lung (14.3)	2006.7 **(140.5)**	950.4 **(66.5)**	278.5 **(19.5)**	8.0 (0.6)
ATG9A	Testis (29.3)	101.7 (3.5)	31.1 (1.1)	33.65 (1.1)	Testis (107.4)	652.8 (6.1)	1474.7 **(13.7)**	573.2 (5.3)	74.6 (0.7)
CKAP4	Smooth muscle (38.0)	63.6 (1.7)	32.1 (0.8)	1333.8 **(35.1)**	Osteoblast day 14 (345.7)	470.7 (1.4)	158.5 (0.5)	7.5 (0.0)	2656.9 (7.7)
DTNA	Below threshold	—	—	—	Lens (4.8)	221.1 **(45.7)**	541.3 **(111.9)**	4.8 (1.0)	39.7 (8.2)
TMEM214	Smooth muscle (150.1)	161.5 (1.1)	193.05 (1.3)	398.05 (2.7)	Lacrimal gland (297.3)	565.5 (1.9)	343.9 (1.2)	605.2 (0.2)	407.6 (1.4)
TMEM38A	[c]	—	—	—	Skeletal muscle (20.4)	1960.8 **(95.9)**	9550.4 **(467.2)**	15.2 (0.7)	29.4 (1.4)

[a] —, not in the BioGPS transcriptome database.
[b] Cell line not studied in the experiment.
[c] Gene not represented in the microarray.

particular, 15 of the low abundance NETs have been directly tested by us and by others (see below and supplemental Table S5) and confirmed at the NE.

Muscle-specific NETs—The identification of new NETs in skeletal muscle that were not in previous liver, blood, and neuroblastoma cell data sets (26–28) could reflect either their preferential expression in muscle or differences in the sensitivity of the mass spectrometers between the time of the different studies. To distinguish between these possibilities, a subset of novel putative rat skeletal muscle NETs was searched for expression levels in the BioGPS transcriptome database that compared relative expression for RNAs from over 60 mouse tissues on microarrays (mouse was used because very little rat transcriptome data were available) (29, 48). Although many NETs were widely expressed according to the transcriptome data, others were preferentially expressed in heart and/or skeletal muscle over other tissues (Fig. 3*A*). A few of these were just 3–10-fold higher in the heart and/or skeletal muscle than the median value for all other tissues, but several reached levels greater than 100-fold over the median value (Fig. 3*A* and Table II). Most of the eight putative NETs shown were expressed at roughly background levels in liver and bone marrow, explaining why they were not found in previous liver (26) or leukocyte (28) NE data sets and further reflecting tissue specificity in the NE proteome.

To confirm these results, qRT-PCR was performed on the same eight muscle NETs over seven human tissues including cardiac and skeletal muscle. Using *GAPDH* as a standard and *CKM* as a positive control, all but *TMX4* were more highly expressed than in liver in at least one of the two muscle tissues (Fig. 3*B*). The results did not precisely match the BioGPS data for which there are many possible explanations, but most of the NETs were preferentially expressed in muscle over several other tissues in both systems.

The tissue specificity of NET expression based on the transcriptome data was not always shared between species (Table II). The BioGPS transcriptome database also compared relative RNA expression levels for over 70 human tissues (29, 48). Some NETs like *WFS1* and *POPDC2* were highly expressed in heart muscle in both human and mouse systems. However, *GPR116* was very preferentially expressed in mouse heart and skeletal muscle yet was expressed at the median level in all human muscle groups (Table II). This may indicate species differences as well as tissue differences in the NE proteome.

Confirmation of NE Residence—To directly test NE residency for novel NETs as a measure of the validity of novel protein identifications, 10 putative NETs from the skeletal muscle data set were cloned as tagged fusions (GFP and/or monomeric red fluorescent protein) and expressed in tissue culture cells. Some were not expressed in the HT1080 cells first used, but when a variety of different cell lines were utilized, all 10 putative NETs were expressed and yielded a discernible rim at the nuclear periphery (Fig. 4*A*). However,

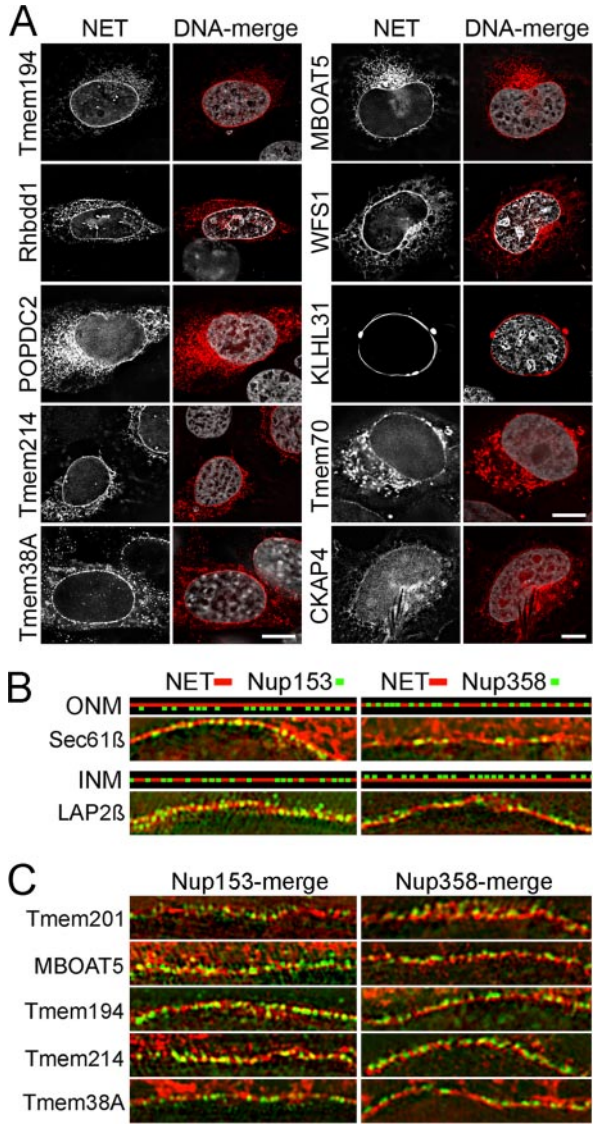

FIG. 4. **Confirmation of NE residence for NETs by targeting tagged fusion proteins.** *A*, NETs were tested as tagged fusions for NE targeting, which is determined by their enrichment in a rim at the limits of DNA staining. NET fusions are visualized in *white* in the *left panels* and in *red* in the *right panels*, whereas DNA is visualized in *white* in the *right panels*. NETs were sometimes expressed or targeted better in certain cell types: all panels shown are U2OS osteosarcoma cells except for TMEM38A in mouse C2C12 cells and TMEM70 and CKAP4 in HeLa cells. All micrographs are on the same scale except for CKAP4 with all *scale bars* at 10 μm. *B* and *C*, inner *versus* outer nuclear membrane targeting. Structured illumination microscopy can distinguish proteins in the INM from those in the ONM when co-stained with nuclear basket protein Nup153 and cytoplasmic filament protein Nup358. *B*, an ONM NET or ER/ONM protein (*red*) should be in the same plane with Nup358 (*green*) but should be external to Nup153 (*green*), and this is observed for the control ER protein Sec61β (*upper schematic* and *images*). Correspondingly, an INM NET should be in the same plane as Nup153 and internal to Nup358 as is observed for the control NET LAP2β (*lower schematic* and *images*). *C*, all new NETs tested appeared in the same plane of the INM with Nup153 and formed an internal ring to Nup358, indicating INM residence. *Bars*, 5 μm.

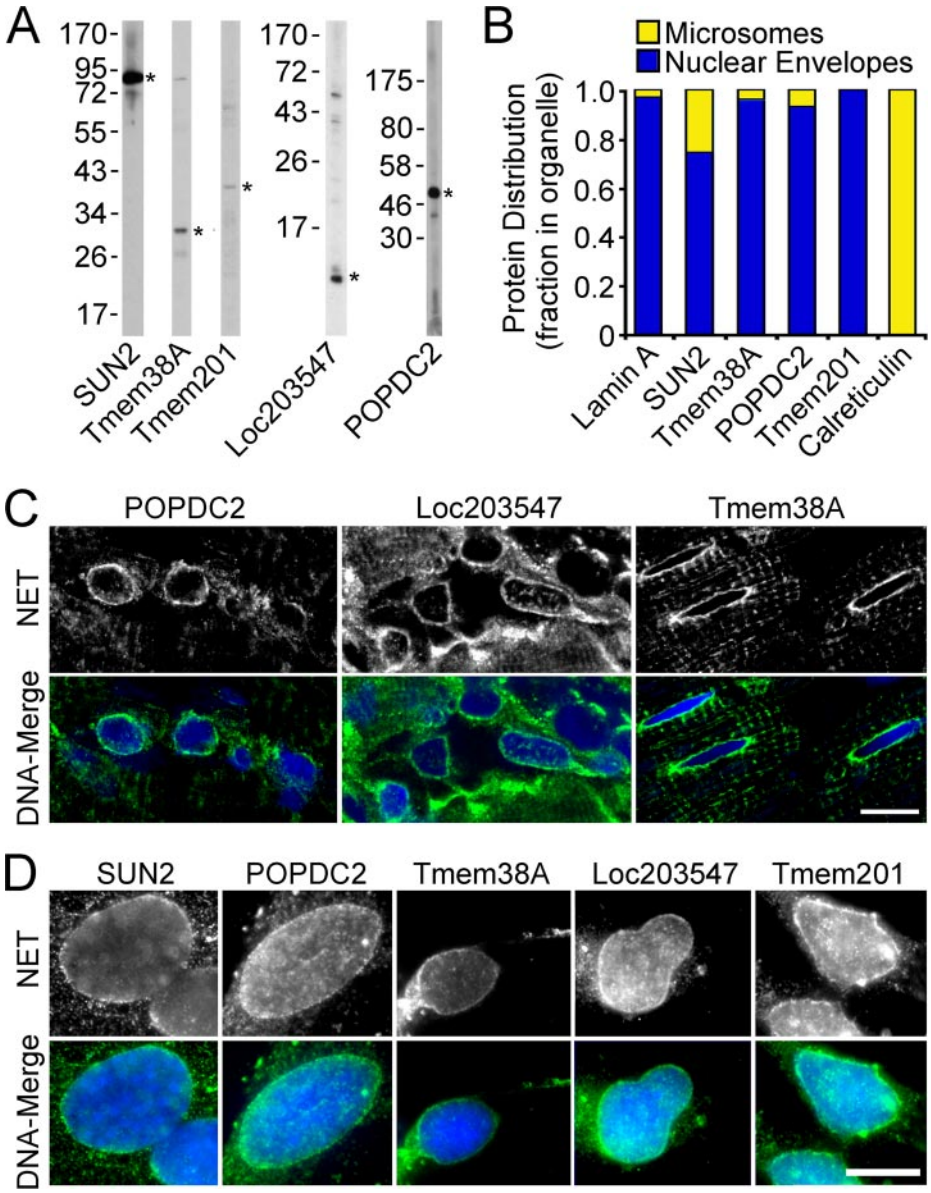

FIG. 5. **Antibody staining confirms novel NET identifications.** *A*, Western blots testing antibodies generated to novel muscle NETs TMEM38A, LOC203547, and POPDC2, control NET SUN2, and a NET previously identified in liver that appears to be much more abundant in muscle, TMEM201/NET5. The correct size for each NET is indicated by an *asterisk*. *B*, comparison of the relative amounts of proteins in ER (microsome) and NE fractions. Lamin A was used as a control for a NE-specific protein, whereas Calreticulin was used as a control for an ER protein. Western blots of the two fractions similarly loaded for total protein were quantified on a LI-COR Odyssey imaging system, and the percentage of the total signal between both microsome and NE lanes was plotted with NE signal in *blue* and microsome signal in *yellow* (three repeats were averaged). The new muscle NETs were more enriched in the NE fraction than was the control NET SUN2. *C*, cryosections of rat muscle stained with NET antibodies. NE staining was clearly observed for all NETs tested as determined by a rim around the DAPI-stained DNA. Leg muscle is shown for TMEM38A, and heart is shown for the other two NETs. *Bars*, 10 μm. *D*, antibody staining on pre-extracted cells. All cells shown are C2C12 mouse myoblasts except in the case of TMEM201 where HeLa cells are shown. Cells were pre-extracted with detergent (1% Triton X-100) to remove membranes and most soluble cytoplasmic material and then fixed and incubated with NET antibodies. A nuclear rim staining was observed for the control NET SUN2 and all novel NETs tested. The resistance to detergent pre-extraction is consistent with the INM localization indicated by OMX results in Fig. 4.

they were quite variable in the percentage of the protein accumulating at the NE. For example, TMEM194 tended to have a very crisp nuclear rim, whereas POPDC2 had higher levels in the cytoplasm, although a rim could still be discerned. Those that had both NE and ER accumulation can be explained by three possibilities. First, binding sites for the NET at the NE might have become saturated due to overexpression, a phenomenon common among NETs. A corollary of this possibility is that partner proteins involved in tethering the NET in the NE are of low abundance in the cell lines used. This

is the possibility we consider most likely because of the high degree of tissue specificity in expression of these NETs. Second, the NET might normally have multiple cellular localizations as a recent proteomics study has suggested for nearly 40% of the mammalian proteome (58). Third, it is possible that the GFP/red fluorescent protein fusion altered the NET protein structure so that it is targeting aberrantly. In this latter case, it is actually more likely that a reduction in affinity at an NE-tethering site results in artifactual accumulation in the ER than that the NE targeting is artifactual, although both are possible. KLHL31 staining was highly filamentous and only sometimes completely encircled the NE. High resolution deconvolved images confirm its proximal association with the NE, but it appeared in some cases of overexpression to concentrate in membrane invaginations protruding into chromatin and in others to form filaments that extended into the cytoplasm beyond the NE.

The NE equally comprises INM and ONM, so NETs could occur in one or the other subcompartment. Structured illumination microscopy (OMX) can distinguish INM from ONM localization by co-staining for proteins from the NPC nuclear basket (Nup153) or cytoplasmic filaments (Nup358) (59). The NPC nuclear basket and cytoplasmic filaments both distend more than 50 nm away from the NE, which itself is roughly 50 nm from the ONM to the INM. Therefore, the combined separation between NETs and these distal NPC components is within the ~100-nm-resolution limit of the OMX system. If a NET is in the ONM, one would observe localization to the same plane as Nup358 and some planar separation with Nup153 (Fig. 4*B*, *upper schematic*), and this is what was observed for the ONM control protein Sec61β (Fig. 4*B*, *upper image*). The reverse should apply for an INM protein with localization to the same plane as Nup153 and some planar separation with Nup358 (Fig. 4*B*, *lower schematic*), and this is what we observed for the INM control protein LAP2β (Fig. 4*B*, *image*). Yellow co-localization is generally not observed in this system because the OMX also resolves the ~120-nm gaps in the nuclear membrane where the NPCs are inserted from the NETs in the membrane itself. Similarly to the control NET LAP2β, all the new skeletal muscle NETs tested here were found to accumulate in the INM as both the NET (*red*) and Nup153 (*green*) localized to the inner ring, whereas an inner NET ring could be distinguished from an outer Nup358 ring (Fig. 4*C*).

To test localization of endogenous protein, polyclonal antibodies were generated to four novel NETs (TMEM38A, POPDC2, LOC203547, and TMEM201). Antibodies were also obtained for the control NET SUN2. Each antibody recognized a protein of the correct size in immunoblots (Fig. 5*A*). Antibodies against each NET were incubated with similar amounts of NE and microsome preparations. Signals from the Western blots were detected with fluorescent antibodies and quantified. The total signal intensity from both NE and microsome bands were measured, and the percentage of total signal for each was plotted. Surprisingly, the control SUN2 had the highest percentage appearing in the microsome fraction (Fig. 5*B*). Thus, when not overexpressed, these novel NETs are more exclusive to the NE than one of the best characterized NETs.

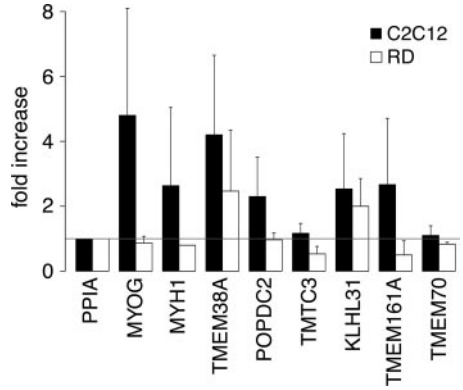

FIG. 6. **NE composition changes during muscle differentiation.** Expression levels of several muscle NETs were tested in both C2C12 (mouse) and RD (human) myoblast to myotube differentiation systems. RNA extracted from both untreated myoblast and chemically differentiated myotube populations were subjected to RT-PCR for each NET, and expression levels were quantified. The relative change between myoblast and myotube populations was determined after first normalizing values to the control peptidylprolyl isomerase A (*PPIA*). Relative transcript levels for both human and mouse systems are shown, and *error bars* indicate standard deviations between three replicates for each differentiation system. Four NETs were induced similarly to positive differentiation controls, *MYOG* and *MYH1*.

POPDC2 and LOC203547 antibodies produced distinctive nuclear rim staining on rat heart muscle cryosections (Fig. 5*C*). The nuclei were clearly visualized with DAPI, and the antibody staining was concentrated in a crisp rim just surrounding the nucleus. The TMEM38A antibodies produced strong nuclear rim staining in rat leg skeletal muscle cryosections in addition to fainter staining in the SR (Fig. 5*C*). This is consistent with supplemental data from a previous report on this protein that introduced it as an SR protein (60). The appearance of TMEM38A in the INM as well as the SR resembles the well characterized NET Emerin that has been reported in the cytoplasm of myotubes and interstitial discs of heart tissue (55, 56, 61). Consistent with the immunofluorescence results, some peptides were obtained in the mass spectrometry analysis of the SR fraction for TMEM38A, Emerin, and SUN2 (supplemental Table S3).

Many previously characterized NETs resist a prefixation extraction with 1% Triton X-100 and 400 mM KCl presumably due to tight associations with the intermediate filament Lamin polymer. The functioning antibodies enabled testing of this on mouse C2C12 myoblast cells. C2C12 cells grown on coverslips were extracted with 1% Triton X-100 prior to fixation. The antibodies concentrated in a rim around the DNA, consistent with retention of these NETs after the detergent preextraction and consistent with observations of INM targeting by OMX. One of the NETs tested, LOC203547, had not been

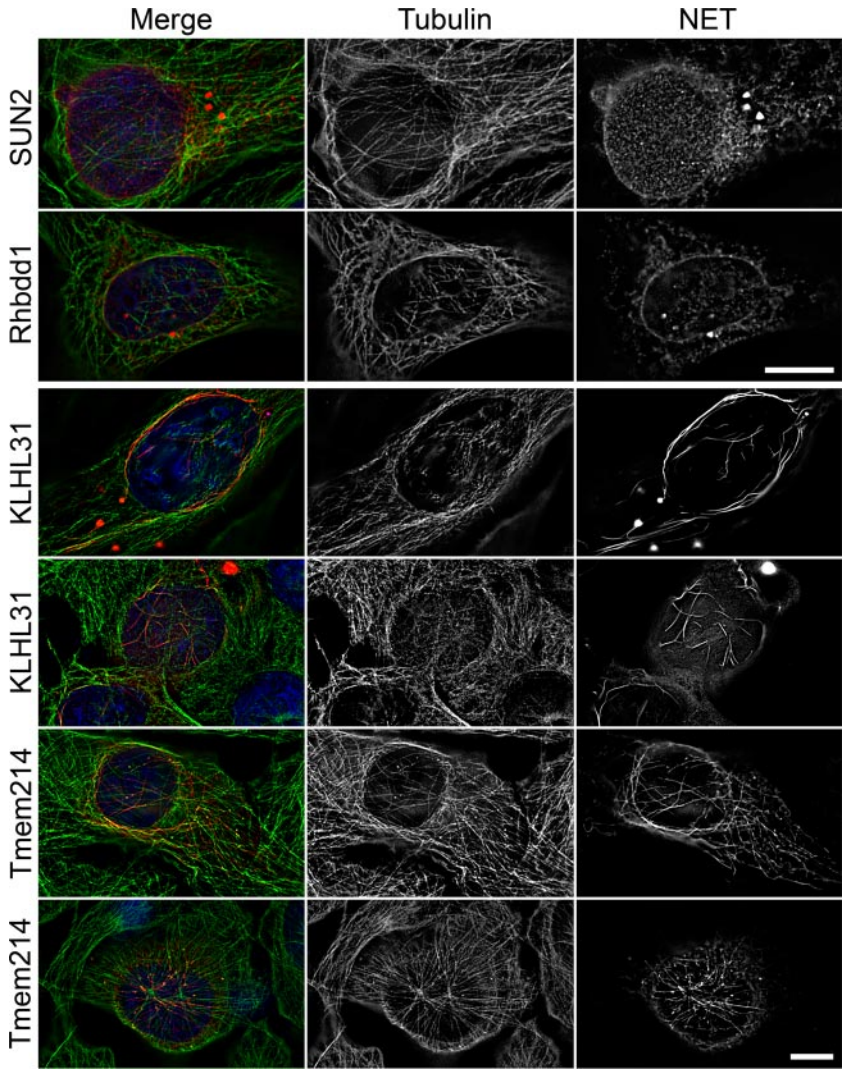

FIG. 7. **Muscle NET alignment with microtubules.** U2OS cells expressing various NET-GFP fusions were fixed and stained for microtubules. Sections from deconvolved images are shown for a focal plane at the upper nuclear surface. DAPI staining for DNA is in *blue*, microtubules are in *green*, and the NET is in *red*. In the *right columns*, the microtubules or NET are shown in *grayscale*. Microtubule filaments are observed crossing the nuclear surface in the SUN2 control-transfected cell, but the SUN2 staining on the surface is spotty, consistent with previous reports. The same was observed for RHBDD1 and most muscle NETs tested; however, KLHL31, which had a more filamentous appearance in Fig. 4, exhibited filaments also on the nuclear surface that partly tracked with the microtubule filaments (note both *grayscale* images for each and some *yellow* co-localization in the *merge panel*). TMEM214, although consistently yielding a much crisper and continuous rim at the nuclear periphery, also exhibited filamentous accumulation at the nuclear surface that exhibited even more overlap with microtubules. *Scale bars*, 10 μm.

cloned or tested by exogenous expression, bringing the number of new NETs with confirmed NE residence to 11. Another of the NETs shown, TMEM201, was previously identified in the liver data set as NET5 (26) but was tested here because it had many more peptides in the skeletal muscle data set (supplemental Table S3).

Several Muscle NETs Are Up-regulated during Muscle Differentiation—Muscle-specific NETs could have functions related to myogenic differentiation. Thus, expression levels of several skeletal muscle NETs were analyzed in myogenic differentiation systems where myoblast cell lines are grown to confluency and then moved to reduced serum medium containing pharmacological agents to induce differentiation. The myoblasts then fuse to form multinucleate myotubes with several characteristics of differentiated muscle. In both human (RD; Ref. 62) and mouse (C2C12; Ref. 63, 64) systems, negative controls were unchanged, whereas *TMEM38A* and *KLHL31* were induced similarly to the positive controls, myogenin (*MYOG*) and myosin heavy chain (*MYH1*) (Fig. 6). *POPDC2* and *TMEM161A* were both up-regulated only in the mouse system. The up-regulation of certain NETs in myogenic differentiation is consistent with their tissue-restricted expression patterns and the fact that the antibodies yielded more distinctive nuclear rim staining in skeletal and heart muscle cryosections than in cell lines.

Three Novel Skeletal Muscle NETs Appear to Associate with the Cytoskeleton—Nesprins 1 and 2 in the ONM bind to the actin cytoskeleton and contribute to nuclear positioning (17), whereas Nesprin 3, originally identified by proteomics of liver NEs (NET53; Ref. 26), binds plectin and thus presumably connects the NE to the intermediate filament cytoskeleton (24). These ONM NETs are also connected to the INM SUN proteins that in turn bind Lamins, hence connecting the cytoskeleton to the nucleoskeleton (15). Thus, NETs in both the ONM and INM are involved in connecting cytoskeletal filaments to the nucleoskeleton. The importance of such connections is illustrated by the recent discovery that mutations in Nesprins 1 and 2 (23) also cause EDMD.

NETs connecting microtubules to the nucleus have not previously been identified, but it is clear that microtubules have some interactions with the NE because they associate with the NE prior to NE disassembly in mitosis (65), and NET5/TMEM201/Samp1 associates with both the centrosome and the mitotic spindle (30, 66). As muscle cells have many unique cytoskeletal features, the novel NETs from skeletal muscle were screened for effects indicating any associations with microtubules.

The NETs were overexpressed in U2OS cells and co-visualized with the microtubule cytoskeleton. Overexpression of most NETs yielded no visible alterations in microtubule organization. However, cell sections at the upper surface of the nucleus revealed a filamentous distribution for KLHL31 and TMEM214 (Fig. 7) in nearly all transfected cells. This strongly contrasted with the typical punctate distribution of NETs at the nuclear surface (SUN2 and RHBDD1 shown). Overlaying the NET and microtubule staining patterns in these sections for KLHL31 and TMEM214 revealed significant co-localization; however, the percentage of microtubules visible at the nuclear surface that tracked with the NETs was highly variable from cell to cell. The *upper* cell for TMEM214 shows also how some of the overexpressed NET distributed in the ER also tracked with the microtubules in the cytoplasm and the lack of a clear microtubule-organizing center. The *lower* cell shows a different defect with two microtubule-organizing centers at the center of the nuclear surface.

Observations of NPC-associated proteins and the NE Lamin proteins on the mitotic spindle (*e.g.* Lamin B, Importin β, and Ran; Refs. 67–69) provided the first evidence that NE proteins have separate roles in mitosis. A more recent study showed that NET5/TMEM201/Samp1 associates with the base of the mitotic spindle in mitosis (30). During mitosis, many NETs are redistributed into small vesicles that spread throughout the cell except from the spindle area. This pattern was observed for most NETs with SUN2 and RHBDD1 shown as examples (Fig. 8). In contrast, TMEM214 exhibited an increased concentration by the spindle base in most cells, although it was excluded from the spindle poles themselves (Fig. 8, *upper right TMEM214 panel*). Some cells exhibited an even more striking microtubule association with clear co-localization throughout the length of many spindle microtubules (Fig. 8, *lower TMEM214 panels*). KLHL31 was distributed differently in mitosis, associating more with the mitotic chromosomes than with microtubules. WFS1, although not tracking with microtubules in interphase, exhibited a distribution similar to that of TMEM214 with a concentration around the base of the spindle in mitosis (Fig. 8, *bottom panels*).

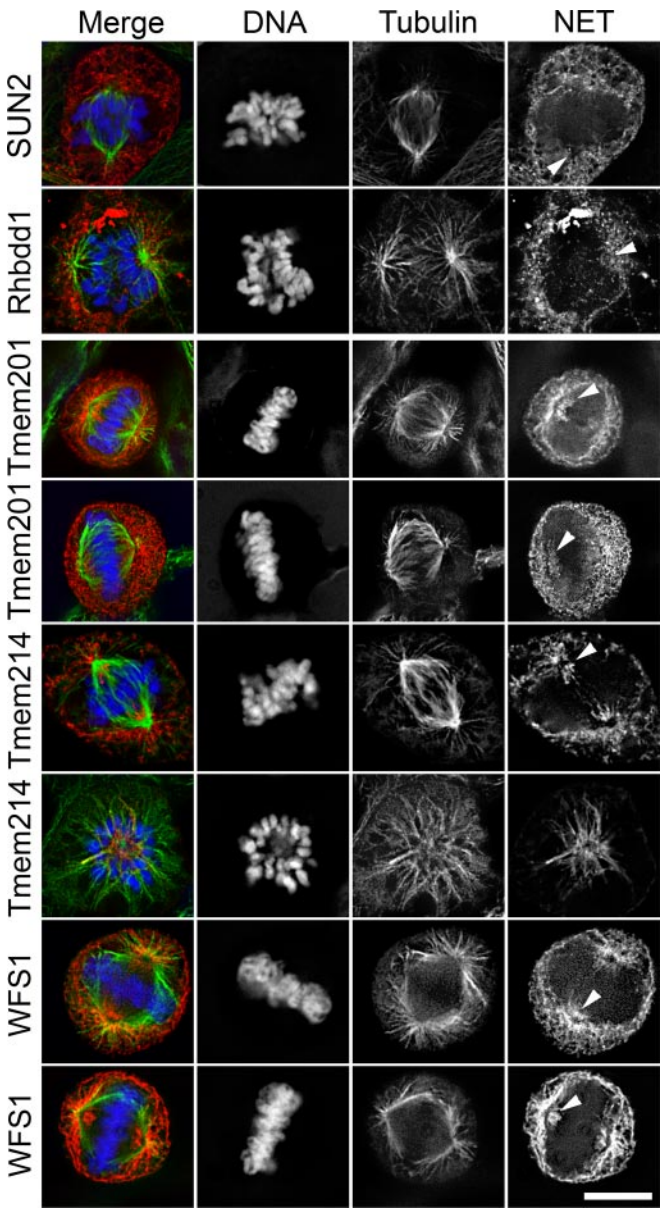

FIG. 8. **Partial NET-microtubule associations are also observed in mitosis.** In mitosis, the NE breaks down, and several NPC proteins and Lamins have previously been reported to partly assemble on the mitotic spindle. The negative control SUN2 and the new muscle-specific NET RHBDD1 were generally distributed throughout the mitotic cell but excluded from the spindle (*white arrowheads* point to one of the spindles in each cell). No particular accumulation or change in the NET distribution was observed with respect to the mitotic spindle. As a positive control, TMEM201 (NET5/Samp1) is shown as it has previously been shown to associate with the spindle. TMEM214 exhibited in most cells a strong accumulation at the base of the spindles close to the poles but was excluded from the poles themselves. In other cells, the distribution was even more focused on the spindle itself with significant co-localization with the microtubules. A third muscle NET, WFS1, consistently yielded the first phenotype of TMEM214; however, in many cases, an even more pronounced accumulation surrounding the spindle poles was observed. One spindle pole in each cell (except the prophase TMEM214 cell) is marked by an *arrowhead*. *Scale bar*, 10 μm.

DISCUSSION

This analysis of the skeletal muscle NE proteome identified many new NE-associated proteins and NETs not identified in earlier studies of liver and neuroblastoma NEs (26, 27) or a more recent study of blood NEs (28). Moreover, some of these

proteins had very restricted tissue expression and were specifically up-regulated in myogenic differentiation systems. Thus, each tissue likely has a different combination of proteins in its NE proteome. That some of these more tissue-restricted NETs track with the microtubule cytoskeleton has the potential to explain some of the tissue specificity of NE disease phenotypes. The three favored hypotheses to explain how NE protein mutation can yield pathology are altered expression of genes regulated from the nuclear periphery, mechanical instability from disruption of lamina-cytoskeleton interactions, and disabling of the cell cycle/stem cell maintenance (6, 7). That NET-microtubule associations indicated here appear to occur in both interphase and mitosis provides potential mechanisms toward both mechanical instability and cell cycle regulation. That some of these proteins are tissue-restricted provides a potential explanation for the tissue preferences in NE disease pathologies.

Much additional work will be required to determine such disease links and whether associations are direct or indirect. Nonetheless, the tracking of TMEM214 and KLHL31 with microtubules on the nuclear surface is both striking and a novel finding among all NETs identified thus far. The association of TMEM214 and WFS1 at the base of the spindles in mitosis resembles that observed for NET5/TMEM201/Samp1 (30). This finding followed observations that Ima1, the yeast homolog of this NET, is involved in connecting the NE to the centrosome (66). Thus, the potential link to cell cycle regulation is even stronger.

The idea of more tissue-specific NETs participating in protein complexes at the NE whose disruption could lead to more muscle-specific pathologies makes sense (70). It is hard otherwise to explain how mutations in ubiquitous proteins like Lamin A, Emerin, or the Nesprin proteins could result in tissue-specific pathologies (18–23). Interestingly, WFS1 has already been linked to three disorders, although the function of the protein remains obscure (71–73). These initial successes in identifying tissue-specific NETs that have links to disease indicate the importance of investigating the NE proteome in all tissues linked to disease.

Acknowledgments—Use of the OMX microscope is supported by the Scottish University Life Sciences Alliance. We thank D. Tollervey and W. C. Earnshaw for comments and F. Melchior, T. Rapoport, E. King, D. Kelly, T. Guan, and S. Mitchell for reagents/technical assistance.

* This study was supported by the Wellcome Trust (senior research fellowship to E. C. S.) and The Stowers Institute for Medical Research (to L. F.).

S This article contains supplemental Figs. S1 and S2 and Tables S1–S5.

§ Both authors contributed equally to this work.

‖ A Royal Society Dorothy Hodgkin fellow.

** A Darwin Trust student.

‡‡ To whom correspondence should be addressed: Wellcome Trust Centre for Cell Biology, University of Edinburgh, Kings Bldgs., Swann 5.22, Mayfield Rd., Edinburgh EH9 3JR, UK. Tel.: 441316507075; Fax: 441316507360; E-mail: e.schirmer@ed.ac.uk.

REFERENCES

1. Prunuske, A. J., and Ullman, K. S. (2006) The nuclear envelope: form and reformation. *Curr. Opin. Cell Biol.* **18,** 108–116
2. Suntharalingam, M., and Wente, S. R. (2003) Peering through the pore: nuclear pore complex structure, assembly, and function. *Dev. Cell* **4,** 775–789
3. Callan, H. G., and Tomlin, S. G. (1950) Experimental studies on amphibian oocyte nuclei. I. Investigation of the structure of the nuclear membrane by means of the electron microscope. *Proc. R. Soc. Lond. B Biol. Sci.* **137,** 367–378
4. Schirmer, E. C., and Foisner, R. (2007) Proteins that associate with lamins: many faces, many functions. *Exp. Cell Res.* **313,** 2167–2179
5. Stewart, C. L., Roux, K. J., and Burke, B. (2007) Blurring the boundary: the nuclear envelope extends its reach. *Science* **318,** 1408–1412
6. Worman, H. J., and Bonne, G. (2007) "Laminopathies": a wide spectrum of human diseases. *Exp. Cell Res.* **313,** 2121–2133
7. Dorner, D., Gotzmann, J., and Foisner, R. (2007) Nucleoplasmic lamins and their interaction partners, LAP2alpha, Rb, and BAF, in transcriptional regulation. *FEBS J.* **274,** 1362–1373
8. Lenz-Böhme, B., Wismar, J., Fuchs, S., Reifegerste, R., Buchner, E., Betz, H., and Schmitt, B. (1997) Insertional mutation of the Drosophila nuclear lamin Dm0 gene results in defective nuclear envelopes, clustering of nuclear pore complexes, and accumulation of annulate lamellae. *J. Cell Biol.* **137,** 1001–1016
9. Liu, J., Rolef Ben-Shahar, T., Riemer, D., Treinin, M., Spann, P., Weber, K., Fire, A., and Gruenbaum, Y. (2000) Essential roles for Caenorhabditis elegans lamin gene in nuclear organization, cell cycle progression, and spatial organization of nuclear pore complexes. *Mol. Biol. Cell* **11,** 3937–3947
10. Lammerding, J., Schulze, P. C., Takahashi, T., Kozlov, S., Sullivan, T., Kamm, R. D., Stewart, C. L., and Lee, R. T. (2004) Lamin A/C deficiency causes defective nuclear mechanics and mechanotransduction. *J. Clin. Investig.* **113,** 370–378
11. Schirmer, E. C., Guan, T., and Gerace, L. (2001) Involvement of the lamin rod domain in heterotypic lamin interactions important for nuclear organization. *J. Cell Biol.* **153,** 479–489
12. Olins, A. L., Herrmann, H., Lichter, P., Kratzmeier, M., Doenecke, D., and Olins, D. E. (2001) Nuclear envelope and chromatin compositional differences comparing undifferentiated and retinoic acid- and phorbol ester-treated HL-60 cells. *Exp. Cell Res.* **268,** 115–127
13. Schirmer, E. C., and Gerace, L. (2004) The stability of the nuclear lamina polymer changes with the composition of lamin subtypes according to their individual binding strengths. *J. Biol. Chem.* **279,** 42811–42817
14. Lammerding, J., Fong, L. G., Ji, J. Y., Reue, K., Stewart, C. L., Young, S. G., and Lee, R. T. (2006) Lamins A and C but not lamin B1 regulate nuclear mechanics. *J. Biol. Chem.* **281,** 25768–25780
15. Crisp, M., Liu, Q., Roux, K., Rattner, J. B., Shanahan, C., Burke, B., Stahl, P. D., and Hodzic, D. (2006) Coupling of the nucleus and cytoplasm: role of the LINC complex. *J. Cell Biol.* **172,** 41–53
16. Starr, D. A., and Fischer, J. A. (2005) KASH 'n Karry: the KASH domain family of cargo-specific cytoskeletal adaptor proteins. *BioEssays* **27,** 1136–1146
17. Starr, D. A., and Han, M. (2002) Role of ANC-1 in tethering nuclei to the actin cytoskeleton. *Science* **298,** 406–409
18. Bonne, G., Di Barletta, M. R., Varnous, S., Bécane, H. M., Hammouda, E. H., Merlini, L., Muntoni, F., Greenberg, C. R., Gary, F., Urtizberea, J. A., Duboc, D., Fardeau, M., Toniolo, D., and Schwartz, K. (1999) Mutations in the gene encoding lamin A/C cause autosomal dominant Emery-Dreifuss muscular dystrophy. *Nat. Genet.* **21,** 285–288
19. Raffaele Di Barletta, M., Ricci, E., Galluzzi, G., Tonali, P., Mora, M., Morandi, L., Romorini, A., Voit, T., Orstavik, K. H., Merlini, L., Trevisan, C., Biancalana, V., Housmanowa-Petrusewicz, I., Bione, S., Ricotti, R., Schwartz, K., Bonne, G., and Toniolo, D. (2000) Different mutations in the LMNA gene cause autosomal dominant and autosomal recessive Emery-Dreifuss muscular dystrophy. *Am. J. Hum. Genet.* **66,** 1407–1412
20. Muchir, A., Bonne, G., van der Kooi, A. J., van Meegen, M., Baas, F., Bolhuis, P. A., de Visser, M., and Schwartz, K. (2000) Identification of mutations in the gene encoding lamins A/C in autosomal dominant limb girdle muscular dystrophy with atrioventricular conduction disturbances (LGMD1B). *Hum. Mol. Genet* **9,** 1453–1459
21. Fatkin, D., MacRae, C., Sasaki, T., Wolff, M. R., Porcu, M., Frenneaux, M.,

Atherton, J., Vidaillet, H. J., Jr., Spudich, S., De Girolami, U., Seidman, J. G., Seidman, C., Muntoni, F., Müehle, G., Johnson, W., and McDonough, B. (1999) Missense mutations in the rod domain of the lamin A/C gene as causes of dilated cardiomyopathy and conduction-system disease. *N. Engl. J. Med.* **341,** 1715–1724

22. Bione, S., Maestrini, E., Rivella, S., Mancini, M., Regis, S., Romeo, G., and Toniolo, D. (1994) Identification of a novel X-linked gene responsible for Emery-Dreifuss muscular dystrophy. *Nat. Genet.* **8,** 323–327
23. Zhang, Q., Bethmann, C., Worth, N. F., Davies, J. D., Wasner, C., Feuer, A., Ragnauth, C. D., Yi, Q., Mellad, J. A., Warren, D. T., Wheeler, M. A., Ellis, J. A., Skepper, J. N., Vorgerd, M., Schlotter-Weigel, B., Weissberg, P. L., Roberts, R. G., Wehnert, M., and Shanahan, C. M. (2007) Nesprin-1 and -2 are involved in the pathogenesis of Emery-Dreifuss muscular dystrophy and are critical for nuclear envelope integrity. *Hum. Mol. Genet* **16,** 2816–2833
24. Wilhelmsen, K., Litjens, S. H., Kuikman, I., Tshimbalanga, N., Janssen, H., van den Bout, I., Raymond, K., and Sonnenberg, A. (2005) Nesprin-3, a novel outer nuclear membrane protein, associates with the cytoskeletal linker protein plectin. *J. Cell Biol.* **171,** 799–810
25. Zhang, Q., Ragnauth, C. D., Skepper, J. N., Worth, N. F., Warren, D. T., Roberts, R. G., Weissberg, P. L., Ellis, J. A., and Shanahan, C. M. (2005) Nesprin-2 is a multi-isomeric protein that binds lamin and emerin at the nuclear envelope and forms a subcellular network in skeletal muscle. *J. Cell Sci.* **118,** 673–687
26. Schirmer, E. C., Florens, L., Guan, T., Yates, J. R., 3rd, and Gerace, L. (2003) Nuclear membrane proteins with potential disease links found by subtractive proteomics. *Science* **301,** 1380–1382
27. Dreger, M., Bengtsson, L., Schöneberg, T., Otto, H., and Hucho, F. (2001) Nuclear envelope proteomics: novel integral membrane proteins of the inner nuclear membrane. *Proc. Natl. Acad. Sci. U.S.A.* **98,** 11943–11948
28. Korfali, N., Wilkie, G. S., Swanson, S. K., Srsen, V., Batrakou, D. G., Fairley, E. A., Malik, P., Zuleger, N., Goncharevich, A., de Las Heras, J., Kelly, D. A., Kerr, A. R., Florens, L., and Schirmer, E. C. (September 13, 2010) The leukocyte nuclear envelope proteome varies with cell activation and contains novel transmembrane proteins that affect genome architecture. *Mol. Cell. Proteomics* 10.1074/mcp.M110.002915
29. Su, A. I., Cooke, M. P., Ching, K. A., Hakak, Y., Walker, J. R., Wiltshire, T., Orth, A. P., Vega, R. G., Sapinoso, L. M., Moqrich, A., Patapoutian, A., Hampton, G. M., Schultz, P. G., and Hogenesch, J. B. (2002) Large-scale analysis of the human and mouse transcriptomes. *Proc. Natl. Acad. Sci. U.S.A.* **99,** 4465–4470
30. Buch, C., Lindberg, R., Figueroa, R., Gudise, S., Onischenko, E., and Hallberg, E. (2009) An integral protein of the inner nuclear membrane localizes to the mitotic spindle in mammalian cells. *J. Cell Sci.* **122,** 2100–2107
31. Wilkie, G. S., and Schirmer, E. C. (2008) Purification of nuclei and preparation of nuclear envelopes from skeletal muscle. *Methods Mol. Biol.* **463,** 23–41
32. Hahn, C. G., and Covault, J. (1990) Isolation of transcriptionally active nuclei from striated muscle using Percoll density gradients. *Anal. Biochem.* **190,** 193–197
33. Florens, L., Korfali, N., and Schirmer, E. C. (2008) Subcellular fractionation and proteomics of nuclear envelopes. *Methods Mol. Biol.* **432,** 117–137
34. Wu, C. C., MacCoss, M. J., Howell, K. E., and Yates, J. R., 3rd (2003) A method for the comprehensive proteomic analysis of membrane proteins. *Nat. Biotechnol.* **21,** 532–538
35. Florens, L., and Washburn, M. P. (2006) Proteomic analysis by multidimensional protein identification technology. *Methods Mol. Biol.* **328,** 159–175
36. McDonald, W. H., Tabb, D. L., Sadygov, R. G., MacCoss, M. J., Venable, J., Graumann, J., Johnson, J. R., Cociorva, D., and Yates, J. R., 3rd (2004) MS1, MS2, and SQT-three unified, compact, and easily parsed file formats for the storage of shotgun proteomic spectra and identifications. *Rapid Commun. Mass. Spectrom.* **18,** 2162–2168
37. Venable, J. D., Dong, M. Q., Wohlschlegel, J., Dillin, A., and Yates, J. R. (2004) Automated approach for quantitative analysis of complex peptide mixtures from tandem mass spectra. *Nat. Methods* **1,** 39–45
38. Eng, J. K., McCormack, A. L., and Yates, J. R., 3rd (1994) An approach to correlate tandem mass spectral data of peptides with amino acid sequences in a protein database. *J. Am. Soc. Mass Spectrom.* **5,** 976–989
39. Tabb, D. L., McDonald, W. H., and Yates, J. R., 3rd (2002) DTASelect and Contrast: tools for assembling and comparing protein identifications from shotgun proteomics. *J. Proteome Res.* **1,** 21–26
40. Zybailov, B. L., Florens, L., and Washburn, M. P. (2007) Quantitative shotgun proteomics using a protease with broad specificity and normalized spectral abundance factors. *Mol. Biosyst.* **3,** 354–360
41. Florens, L., Carozza, M. J., Swanson, S. K., Fournier, M., Coleman, M. K., Workman, J. L., and Washburn, M. P. (2006) Analyzing chromatin remodeling complexes using shotgun proteomics and normalized spectral abundance factors. *Methods* **40,** 303–311
42. Paoletti, A. C., Parmely, T. J., Tomomori-Sato, C., Sato, S., Zhu, D., Conaway, R. C., Conaway, J. W., Florens, L., and Washburn, M. P. (2006) Quantitative proteomic analysis of distinct mammalian Mediator complexes using normalized spectral abundance factors. *Proc. Natl. Acad. Sci. U.S.A.* **103,** 18928–18933
43. Zybailov, B., Mosley, A. L., Sardiu, M. E., Coleman, M. K., Florens, L., and Washburn, M. P. (2006) Statistical analysis of membrane proteome expression changes in Saccharomyces cerevisiae. *J. Proteome Res.* **5,** 2339–2347
44. Zhang, Y., Wen, Z., Washburn, M. P., and Florens, L. (2010) Refinements to label free proteome quantitation: how to deal with peptides shared by multiple proteins. *Anal. Chem.* **82,** 2272–2281
45. Flicek, P., Aken, B. L., Beal, K., Ballester, B., Caccamo, M., Chen, Y., Clarke, L., Coates, G., Cunningham, F., Cutts, T., Down, T., Dyer, S. C., Eyre, T., Fitzgerald, S., Fernandez-Banet, J., Gräf, S., Haider, S., Hammond, M., Holland, R., Howe, K. L., Howe, K., Johnson, N., Jenkinson, A., Kähäri, A., Keefe, D., Kokocinski, F., Kulesha, E., Lawson, D., Longden, I., Megy, K., Meidl, P., Overduin, B., Parker, A., Pritchard, B., Prlic, A., Rice, S., Rios, D., Schuster, M., Sealy, I., Slater, G., Smedley, D., Spudich, G., Trevanion, S., Vilella, A. J., Vogel, J., White, S., Wood, M., Birney, E., Cox, T., Curwen, V., Durbin, R., Fernandez-Suarez, X. M., Herrero, J., Hubbard, T. J., Kasprzyk, A., Proctor, G., Smith, J., Ureta-Vidal, A., and Searle, S. (2008) Ensembl 2008. *Nucleic Acids Res.* **36,** D707–D714
46. Krogh, A., Larsson, B., von Heijne, G., and Sonnhammer, E. L. (2001) Predicting transmembrane protein topology with a hidden Markov model: application to complete genomes. *J. Mol. Biol.* **305,** 567–580
47. Carbon, S., Ireland, A., Mungall, C. J., Shu, S., Marshall, B., and Lewis, S. (2009) AmiGO: online access to ontology and annotation data. *Bioinformatics* **25,** 288–289
48. Wu, C., Orozco, C., Boyer, J., Leglise, M., Goodale, J., Batalov, S., Hodge, C. L., Haase, J., Janes, J., Huss, J. W., 3rd, and Su, A. I. (2009) BioGPS: an extensible and customizable portal for querying and organizing gene annotation resources. *Genome Biol.* **10,** R130
49. Mootha, V. K., Bunkenborg, J., Olsen, J. V., Hjerrild, M., Wisniewski, J. R., Stahl, E., Bolouri, M. S., Ray, H. N., Sihag, S., Kamal, M., Patterson, N., Lander, E. S., and Mann, M. (2003) Integrated analysis of protein composition, tissue diversity, and gene regulation in mouse mitochondria. *Cell* **115,** 629–640
50. Apel, E. D., Lewis, R. M., Grady, R. M., and Sanes, J. R. (2000) Syne-1, a dystrophin- and Klarsicht-related protein associated with synaptic nuclei at the neuromuscular junction. *J. Biol. Chem.* **275,** 31986–31995
51. Hodzic, D. M., Yeater, D. B., Bengtsson, L., Otto, H., and Stahl, P. D. (2004) Sun2 is a novel mammalian inner nuclear membrane protein. *J. Biol. Chem.* **279,** 25805–25812
52. Manilal, S., Nguyen, T. M., Sewry, C. A., and Morris, G. E. (1996) The Emery-Dreifuss muscular dystrophy protein, emerin, is a nuclear membrane protein. *Hum. Mol. Genet.* **5,** 801–808
53. Worman, H. J., Yuan, J., Blobel, G., and Georgatos, S. D. (1988) A lamin B receptor in the nuclear envelope. *Proc. Natl. Acad. Sci. U.S.A.* **85,** 8531–8534
54. Zhang, Q., Skepper, J. N., Yang, F., Davies, J. D., Hegyi, L., Roberts, R. G., Weissberg, P. L., Ellis, J. A., and Shanahan, C. M. (2001) Nesprins: a novel family of spectrin-repeat-containing proteins that localize to the nuclear membrane in multiple tissues. *J. Cell Sci.* **114,** 4485–4498
55. Cartegni, L., di Barletta, M. R., Barresi, R., Squarzoni, S., Sabatelli, P., Maraldi, N., Mora, M., Di Blasi, C., Cornelio, F., Merlini, L., Villa, A., Cobianchi, F., and Toniolo, D. (1997) Heart-specific localization of emerin: new insights into Emery-Dreifuss muscular dystrophy. *Hum. Mol. Genet* **6,** 2257–2264
56. Lattanzi, G., Ognibene, A., Sabatelli, P., Capanni, C., Toniolo, D., Columbaro, M., Santi, S., Riccio, M., Merlini, L., Maraldi, N. M., and Squarzoni,

S. (2000) Emerin expression at the early stages of myogenic differentiation. *Differentiation* **66,** 208–217
57. Salpingidou, G., Smertenko, A., Hausmanowa-Petrucewicz, I., Hussey, P. J., and Hutchison, C. J. (2007) A novel role for the nuclear membrane protein emerin in association of the centrosome to the outer nuclear membrane. *J. Cell Biol.* **178,** 897–904
58. Foster, L. J., de Hoog, C. L., Zhang, Y., Zhang, Y., Xie, X., Mootha, V. K., and Mann, M. (2006) A mammalian organelle map by protein correlation profiling. *Cell* **125,** 187–199
59. Schermelleh, L., Carlton, P. M., Haase, S., Shao, L., Winoto, L., Kner, P., Burke, B., Cardoso, M. C., Agard, D. A., Gustafsson, M. G., Leonhardt, H., and Sedat, J. W. (2008) Subdiffraction multicolor imaging of the nuclear periphery with 3D structured illumination microscopy. *Science* **320,** 1332–1336
60. Yazawa, M., Ferrante, C., Feng, J., Mio, K., Ogura, T., Zhang, M., Lin, P. H., Pan, Z., Komazaki, S., Kato, K., Nishi, M., Zhao, X., Weisleder, N., Sato, C., Ma, J., and Takeshima, H. (2007) TRIC channels are essential for Ca^{2+} handling in intracellular stores. *Nature* **448,** 78–82
61. Wheeler, M. A., Warley, A., Roberts, R. G., Ehler, E., and Ellis, J. A. (2010) Identification of an emerin-beta-catenin complex in the heart important for intercalated disc architecture and beta-catenin localisation. *Cell. Mol. Life Sci.* **67,** 781–796
62. McAllister, R. M., Melnyk, J., Finkelstein, J. Z., Adams, E. C., Jr., and Gardner, M. B. (1969) Cultivation in vitro of cells derived from a human rhabdomyosarcoma. *Cancer* **24,** 520–526
63. Blau, H. M., Pavlath, G. K., Hardeman, E. C., Chiu, C. P., Silberstein, L., Webster, S. G., Miller, S. C., and Webster, C. (1985) Plasticity of the differentiated state. *Science* **230,** 758–766
64. Yaffe, D., and Saxel, O. (1977) Serial passaging and differentiation of myogenic cells isolated from dystrophic mouse muscle. *Nature* **270,** 725–727
65. Salina, D., Bodoor, K., Eckley, D. M., Schroer, T. A., Rattner, J. B., and Burke, B. (2002) Cytoplasmic dynein as a facilitator of nuclear envelope breakdown. *Cell* **108,** 97–107
66. King, M. C., Drivas, T. G., and Blobel, G. (2008) A network of nuclear envelope membrane proteins linking centromeres to microtubules. *Cell* **134,** 427–438
67. Ohba, T., Nakamura, M., Nishitani, H., and Nishimoto, T. (1999) Self-organization of microtubule asters induced in Xenopus egg extracts by GTP-bound Ran. *Science* **284,** 1356–1358
68. Tsai, M. Y., Wang, S., Heidinger, J. M., Shumaker, D. K., Adam, S. A., Goldman, R. D., and Zheng, Y. (2006) A mitotic lamin B matrix induced by RanGTP required for spindle assembly. *Science* **311,** 1887–1893
69. Wiese, C., Wilde, A., Moore, M. S., Adam, S. A., Merdes, A., and Zheng, Y. (2001) Role of importin-beta in coupling Ran to downstream targets in microtubule assembly. *Science* **291,** 653–656
70. Wilkie, G. S., and Schirmer, E. C. (2006) Guilt by association: the nuclear envelope proteome and disease. *Mol. Cell. Proteomics* **5,** 1865–1875
71. Bespalova, I. N., Van Camp, G., Bom, S. J., Brown, D. J., Cryns, K., DeWan, A. T., Erson, A. E., Flothmann, K., Kunst, H. P., Kurnool, P., Sivakumaran, T. A., Cremers, C. W., Leal, S. M., Burmeister, M., and Lesperance, M. M. (2001) Mutations in the Wolfram syndrome 1 gene (WFS1) are a common cause of low frequency sensorineural hearing loss. *Hum. Mol. Genet.* **10,** 2501–2508
72. Domènech, E., Gómez-Zaera, M., and Nunes, V. (2002) WFS1 mutations in Spanish patients with diabetes mellitus and deafness. *Eur. J. Hum. Genet.* **10,** 421–426
73. Strom, T. M., Hörtnagel, K., Hofmann, S., Gekeler, F., Scharfe, C., Rabl, W., Gerbitz, K. D., and Meitinger, T. (1998) Diabetes insipidus, diabetes mellitus, optic atrophy and deafness (DIDMOAD) caused by mutations in a novel gene (wolframin) coding for a predicted transmembrane protein. *Hum. Mol. Genet.* **7,** 2021–2028